Topological properties of mono- and multilayer graphene, flat bands and surface superconductivity

Terhi Moisala
August 7, 2015

Master's Thesis

University of Jyväskylä
Department of Physics

Supervisor: Tero T. Heikkilä

Acknowledgements

I would like to acknowledge Professor Tero Heikkilä for an interesting topic and motivated supervision. I would also like to thank my friends and family for useful conversations and support.

Abstract

In this thesis I study the symmetries and topological properties of graphene and rhombohedral graphite. To break the sublattice symmetry of graphene I add a staggering potential α to the model. I study the effect of α in graphite by calculating the low energy dispersion relations in the bulk and on the surfaces. I get as a result that α opens up a gap to the surface states of graphite, but retains the form of a flat band obtained in [16].

I also study the superconducting surface states of rhombohedral graphite in the presence of a staggering potential. I get that the staggering potential breaks the symmetry between the surface layers and produces different order parameters for the two surfaces in the presence of non-zero chemical potential. The asymmetry can be tuned with suitable doping such that the superconductivity occurs only on the other surface. I also obtain a peculiar asymmetry in the numerical solutions for the order parameters even for zero doping, that cannot be explained by the theory. This may be a metastable state or a numerical issue, that should be analysed in detail in future studies.

Tiivistelmä

Tutustun Pro Gradu -työssäni topologisiin materiaaleihin ja perehdyn grafeenin sekä romboedrisen grafiitin ominaisuuksiin tästä näkökulmasta. Erityisesti tutkin grafeenin alihilasymmetrian rikkoutumisen vaikutuksia grafiitissa lisäämällä heilahtelevan potentiaalin α grafeenin tight-binding -malliin. Lasken romboedrisen grafiitin matalaenergiatilat tight-binding -mallista ja saan tulokseksi, että α avaa energia-aukon, mutta säilyttää vyön tasomaisen muodon, joka on saatu artikkelissa [16].

Tutkin työssäni myös heilahtelevan potentiaalin vaikutusta romboedrisen grafiitin suprajohtaviin pintatiloihin. Päätulokseni on, että heilahteleva potentiaali rikkoo grafiitin pintojen välisen symmetrian ja tuottaa näille eri järjestysparametrit, kun systeemillä on äärellinen kemiallinen potentiaali. Muuttamalla kemiallista potentiaalia epäsymmetriaa voidaan kasvattaa niin, että suprajohtavuutta esiintyy vain toisella pinnalla. Saan lisäksi numeerisesta analyysistä epäsymmetriset ratkaisut myös silloin, kun kemiallista potentiaalia ei ole, mitä ei voida selittää tämän mallin avulla. Kyseessä saattaa olla metastabiili tila tai täysin numeerinen ongelma, jonka analyysin jätän myöhempiin tutkimuksiin.

Contents

1 Introduction

This thesis contains the theoretical basics and some mutual connections of three hot topics in condensed matter physics: graphene, superconductivity and topological materials. The first of these is the most studied material of the psast decade. Theoretically many of its peculiar properties, such as incredible strength and excellent electrical and thermal conductivities, have been known for a long time. It is also very common in nature, since the well known form of carbon, graphite, is actually just multilayer graphene. The reason why graphene has aroused such great interest only recently is the fact that it is very hard to produce, since the thickness of a graphene layer is only one atom. However, ever since the method of detaching graphene was invented in 2003 the properties of graphene and possible applications have been researched.

Also superconductivity is a topic that has attracted a lot of attention among materials scientists. Unlike graphene, the phenomenon of superconductivity has been known for over a century but the mechanism behind it remains still partly an open question. It took almost fifty years from the best physicists of that time to formulate the BCS-theory that we today regard as the basic theory of superconductivity. Nevertheless the BCS-theory cannot explain the origin of high-temperature superconductivity that is still under investigation.

The two topics, properties of graphene and superconductivity, are united in an interesting way as recent experiments suggest graphite to support high-temperature superconductivity [1, 4, 5, 19]. These results motivated this work that follows and widens the calculations in [16]. The origin of the superconductivity may be explained in terms of topological materials, a new field of condensed matter physics. According to [16] the superconductivity is a result of the topological properties of graphite that lead to a formation of a flat band, a disc of zero modes on the surface of graphite. Topological materials are states that cannot be defined purely through the symmetries of the system, but the full description demands also the consideration of global properties such as the topology of the energy bands. These properties can be quantified with different topological invariants that describe the topological order of the state.

This thesis is organized as follows. First I introduce the concept of topological materials. I begin with a brief introduction to the theoretical formalism behind the topological invariants and describe then qualitatively the characterizing properties of topological insulators and topological semimetals. In the following section I present the tight-binding model of graphene and derive the linear dispersion around the Dirac points. Symmetries and topological properties of graphene are also discussed and the breaking of inversion symmetry is demonstrated by adding a staggering potential into the system. These calculations serve as a starting point to the treatment of graphite that takes place

in section 4. I derive the energy dispersion in the bulk and on the surface in the presence of the staggering potential from the tight-binding model and analyse the results also in the concept of topological materials. In section 5 the BCS theory of superconductivity is introduced and in section 6 I write the superconducting Hamiltonian for graphite based on the BCS-theory. From there I derive the energy dispersion for the superconducting surface states of graphite and the self-consistency equation for the order parameter Δ. Finally I discuss the effect of the staggering potential on the superconductivity on the graphite surfaces.

2 Topological materials

Understanding different phases of matter is one of the oldest and most important goals of condensed matter physics. The most common phases, such as crystal or liquid, can be understood classically by how the atoms are organized in the materials. This kind of description is clearly insufficient for quantum based phases such as ferromagnets, superconductors and Bose-Einstein condensates. In 1940's Lev Landau stated that the phase of matter is determined by the symmetries of the quantum state. He also connected the concept of the order parameter to the phase transition in a clear, quantitative way. For example, a transition of a metal into a ferromagnet can be understood as a spontaneous breaking of rotational symmetry of the spin as magnetization sets the specific direction of the north pole. The order parameter of magnetization is spin polarization vector which vanishes above a certain critical temperature.

For a long time physicists believed that the Landau symmetry-breaking theory describes all the possible orders and phase transitions in materials. However, in 1980 it was experimentally verified that the quantum Hall effect gives rise to exactly quantized Hall conductance. The existence of this kind of state could not be explained by symmetry arguments, contrary to Landau theory. This motivated Thouless to introduce the concept of topological order [22]. Later a wide class of materials has been found that can be characterized rather by topology than by symmetries, such as fractional quantum Hall states and topological insulators. At the moment topological materials are of a great interest to materials scientists and the theory describing them is still incomplete; by now a Landau-like theory for a non-local order parameter has not been developed. New proposals for topological materials are constantly searched for among studying the already known ones.

2.1 Berry phase

The whole field of topological materials originates from a physical phenomenon called geometrical phase or *Berry phase*. In 1984 Michael Berry presented in his article that during a cyclic adiabatic process a quantum state gains, in addition to the dynamical phase, a gauge invariant phase factor that depends on the geometry of the parameter space. Apart from solid-state physics, the Berry phase effects in various fields of physics have close analogues to differential geometry and gauge field theories. In this section I introduce the theoretical description of Berry phase and other physical entities that naturally arise, such as Berry curvature and Chern number, following review [26].

Assume we have a physical system described by Hamiltonian $H(\mathbf{R}(t))$ that depends on time through a vector parameter $\mathbf{R} = (R_1, R_2, ...)$ in parameter space

$\mathcal{M}_{\mathbf{R}}$. The system has orthonormal eigenstates $|\psi_n(\mathbf{R})\rangle$ such that

$$H(\mathbf{R})\,|\psi_n(\mathbf{R})\rangle = \epsilon_n(\mathbf{R})\,|\psi_n(\mathbf{R})\rangle\,. \tag{1}$$

According to the adiabatic theorem (see Appendix A), if the system is initially on the eigenstate $|\psi_i(\mathbf{R}(0))\rangle$, it will end up in an adiabatic process to a state

$$|\psi(t)\rangle = e^{i\gamma_i} e^{i\delta_i(t)}\,|\psi_i(\mathbf{R}(0))\rangle\,, \tag{2}$$

where

$$\delta_i(t) = -\frac{1}{\hbar}\int_0^t \mathrm{d}t'\epsilon_i(\mathbf{R}(t')) \quad \text{and} \quad \gamma_i(t) = \int_{\mathcal{C}} \mathrm{d}\mathbf{R}\cdot\mathbf{A}_i(\mathbf{R}). \tag{3}$$

Above the second exponential $\delta_i(t)$ is known as the dynamical phase and it arises from the time evolution of the system. The "extra" phase factor $e^{i\gamma_i(t)}$ depends only on the path $\mathcal{C}$ the system travels in the parameter space and the Berry vector potential

$$\mathbf{A}_n(\mathbf{R}) = i\,\langle\psi_n(\mathbf{R}(0))|\,\nabla_{\mathbf{R}}\,|\psi_n(\mathbf{R}(0))\rangle\,. \tag{4}$$

It is also gauge dependent, since in a gauge transformation

$$|\psi_n(\mathbf{R}(t))\rangle \to e^{i\xi(\mathbf{R})}\,|\psi_n(\mathbf{R}(t))\rangle \tag{5}$$

it transforms as

$$\mathbf{A}_n(\mathbf{R}) \to \mathbf{A}_n(\mathbf{R}) - \nabla_{\mathbf{R}}\xi(\mathbf{R}). \tag{6}$$

Until 1984 the phase γ_n had been omitted as non-physical, since one can always choose a gauge such that it cancels out. However, if the path $\mathcal{C}$ is chosen to be closed, i.e. $\mathbf{R}(t) = \mathbf{R}(0)$, it becomes a gauge-invariant physical quantity

$$\gamma_n(t) = \oint_{\mathcal{C}} \mathrm{d}\mathbf{R}\cdot\mathbf{A}_n(\mathbf{R}) \tag{7}$$

and is called the Berry phase.

2.2 Chern number

From Eq. (6) one can make an interesting remark, namely the vector potential $\mathbf{A}_n(\mathbf{R})$ transforms in a gauge transformation exactly as the electrodynamic vector potential. That encourages us to rewrite Eq. (7) using Stokes' theorem and get

$$\gamma_n(t) = \int_{\mathcal{S}} \mathrm{d}\mathbf{S}\cdot\Omega_n(\mathbf{R}) \tag{8}$$

with

$$\Omega_n(\mathbf{R}) = \nabla_{\mathbf{R}} \times \mathbf{A}_n(\mathbf{R}). \tag{9}$$

The quantity $\Omega_n(\mathbf{R})$ is called *Berry curvature*. Here the cross product symbol $\times$ is used in order to see the analogue to a magnetic field in the parameter space. In general we should use contraction with the Levi-Civita symbol ϵ_{ijk}. Berry curvature is thus a tensor that corresponds to the gauge-field tensor in electrodynamics. Unlike Berry vector potential, Berry curvature is gauge independent and thus an observable. It is also a local quantity that depends only on the geometry of the parameter space whereas Berry phase depends on the chosen path.

For numerical purposes and to get further insight into the nature of Berry curvature, we may write Eq. (9) in the form [26]

$$\Omega_n(\mathbf{R}) = i \sum_{n \neq m} \frac{\langle \psi_n(\mathbf{R}) | \nabla_{\mathbf{R}} H(\mathbf{R}) | \psi_m(\mathbf{R}) \rangle \times \langle \psi_m(\mathbf{R}) | \nabla_{\mathbf{R}} H(\mathbf{R}) | \psi_n(\mathbf{R}) \rangle}{(\epsilon_n(\mathbf{R}) - \epsilon_m(\mathbf{R}))^2} \tag{10}$$

assuming the states form a complete set of eigenstates. In the adiabatic approximation, presented in Appendix A, we essentially project out all the other energy states but the initial one. In other words, we assume that the system is restricted to the nth energy level. The effect of the projected-out energy levels manifests itself as Berry curvature. Especially, if the initial state is degenerated at some value $\mathbf{R}(t)$, then $\Omega_n(\mathbf{R})$ becomes singular. So degeneracy points of the energy levels act as sources or drains of the Berry curvature flux.

Let us consider the case where the parameter space $\mathcal{M}_{\mathbf{R}}$ is a two dimensional compact manifold. Then the integration of the Berry curvature over the parameter space gives the number of monopoles in units of 2π. The integer

$$C_n = \frac{1}{2\pi} \int_{\mathcal{M}_{\mathbf{R}}} \mathrm{d}\mathbf{R}\, \Omega_n(\mathbf{R}). \tag{11}$$

is called the *Chern number*. This number proves to have a deep physical and mathematical meaning and it is the origin of several quantization effects, such as Hall conductance. A non-zero Chern number means that the Berry Curvature has singularities in points of parameter space, or equivalently, that we are not able to find a gauge in which all the wavefunctions are well defined [2]. A more intuitive analogue can be found in differential geometry. For an orientable surface S we can define a topological invariant g, genus, which essentially counts the number of holes in the manifold. On the other hand, the geometrical properties of the surface on a point are characterized by a quantity called the Gaussian curvature K. It is defined as a product of principal curvatures $K = \kappa_1 \kappa_2$ that are

the minimum and maximum of the normal curvatures. If the Gaussian curvature is positive the surface is dome like whereas for a negative value it is saddle shaped. There is a deep connection between the variables g and K, which is formulated by the Gauss-Bonnet theorem. It states that the integral of the Gaussian curvature over the surface gives an integer

$$\chi = \frac{1}{2\pi} \int_S \mathrm{d}A\, K \tag{12}$$

called the Euler characteristic, which is related to the genus by $\chi = 2 - 2g$ [14] if the surface S is closed. The similarity with equation (11) is obvious.

A crucial observation is that also the Chern number is indeed a topological invariant. Genus and then Euler characteristic uniquely define the topology of a compact orientable surface [21]. In topological band theory the parameter space is the Brillouin zone in the reciprocal space. Due to the periodical boundary conditions, the d-dimensional Brillouin zone is homeomorphic to a torus T^d in d dimensions, which is a compact surface in $\mathbb{R}^d$. Hence the Chern number can be used to characterize topologically distinct phases of matter.

2.3 Topological insulators

The topological insulators are a class of topological materials that can be described by the topological band theory. They are indeed insulators: they have an energy gap between the valence and conduction bands. Two insulators are stated to be topologically equivalent if they can be deformed into another by an adiabatic change of the Hamiltonian. In practice this means that the energy gap must remain finite through the transformation, which sets the upper limit for the speed of the transformation. The existence of the gap leads to the fact that the topology of the band is robust against small perturbations, presuming the perturbations respect the crucial symmetries of the system. The band may be moved or transformed, but as long as the perturbation does not close the gap the state remains in the same equivalence class.

In addition to the energy gap a topological insulator must posses a non-trivial topological order, i.e., it has a non-zero topological invariant. In the case of the quantum Hall state this topological invariant is the Chern number. Often the topological insulators characterized by the quantum Hall state are called Chern insulators. The best known example was presented by Haldane already in 1988 [8]. He showed that breaking the time-reversal symmetry in graphene gives rise to a finite Chern number and the quantum Hall effect. The non-trivialness of a topological insulator arises from a topological defect in the reciprocal space called the magnetic skyrmion. A visualization of a skyrmion is

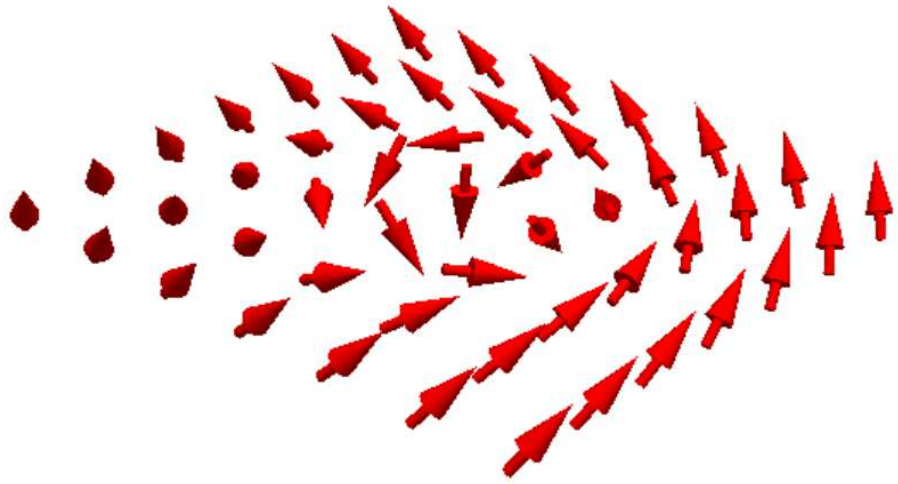

Figure 1: Skyrmion

in Fig. 1. Because of the topological defect no continuous, global, smooth gauge can be chosen in the Brillouin zone. This gives rise to non-zero Chern number as stated above. Due to their magnetic nature, skyrmions cannot exist in the presence of time reversal symmetry. Hence, all the Chern insulators break the time-reversal symmetry.

Also other types of topological invariants exist. In the presence of time reversal symmetry a different topological class of insulating band structures is allowed by spin orbit interaction. This topological order is characterized by $\mathbb{Z}_2$ invariant, which has many similarities to the Chern number. The two possible values $\nu = 0,1$ define if the insulator is topologically trivial or not. In a two dimensional system that is invariant under spin rotations along the z-axis the $\mathbb{Z}_2$ invariant has a straightforward connection to the Chern number. In that case the Hamiltonian separates for up and down spins and the resulting blocks $H_\uparrow$, $H_\downarrow$ have independent Chern integers $C_n^\uparrow$ and $C_n^\downarrow$. Their sum is zero due to the time reversal symmetry, but the difference $C_n^\sigma = (C_n^\uparrow - C_n^\downarrow)/2$ is not necessarily. Then the $\mathbb{Z}_2$ invariant is $\nu = C_n^\sigma \bmod 2$. This quantity tells if the system possesses quantized spin Hall conductivity. [14].

2.4 Bulk-boundary correspondence

A fundamental consequence of topologically non-trivial bulk modes is the existence of conducting chiral edge states. This property is so specific to the topological insulators that it can be even used to characterize them instead of the

bulk Chern number. Phenomenologically the origin of the gapless states at the interface of topologically different insulators can be understood as follows: if the gap would remain finite over the boundary, the two materials would actually belong to the same topological equivalence class by the definition given above. These edge states are said to be *topologically protected* since they cannot be removed by small perturbations that preserve the essential symmetries in the bulk.

A priori it is not clear that the topological equivalence classes given by the Chern number are the same as the ones defined by the band topology. This can be justified by the fact that the Chern number is always integer valued. Clearly, if two Hamiltonians have different Chern numbers they cannot be continuously deformed into each other or otherwise at some point the Chern number would not be well defined. The difference in the Chern number across the edge can also be used to characterize the edge states. Historically Thouless understood the significance of the topological order particularly through the conducting edge states of the quantum Hall state. He noticed that the quantized Hall conductance at the edge is given by the Chern number. For a two-dimensional topological insulator it can be derived that at the interface [7]

$$\Delta C_n = N_R - N_L \,, \tag{13}$$

where $N_{R,L}$ are the numbers of right and left moving chiral edge modes that cross the Fermi level and connect the bulk valence and conduction bands [2]. So at the boundary of insulators with different topological invariants there must be at least one zero mode. The characterizing property of quantum Hall effect, the perfectly quantized conductance, is explained by the chirality of the modes. Since there are only states propagating in one direction, there are no sates for backscattering and the current is insensitive to disorder [14].

2.5 Topological semimetals

The exploration of free Fermion topological insulators has gone on for a few years and their basic properties begin to be well understood. Quite recently researchers have started to investigate generalizations for the topological insulators. For example, can there be a non-trivial topological phase where the gap is not complete but the bands touch at points of the Brillouin zone? Turns out that there is a class of materials, called *topological semimetals*, for which the band topology can be defined despite the absence of the gap. This appears inconsistent as the definition of the band topology relies on the fact that perturbations do not essentially change the properties of a fully gapped system. However, in the case of topological semimetals the robustness of the phase arises from

the topological protection of the band touchings. These gapless points form a subspace in the Brillouin zone called the *nodal space*. Typically they are single points, nodes, or form an arc in which case the nodal space is called the nodal line.

The existence of topological semimetals is closely related to the physics of topological insulators. In fact, the topologically protected gapless states can be seen as surface states of a topological insulator derived from a submanifold of the Brillouin zone surrounding the nodal space. If also the dimension of the nodal space q and the dimension of the system d are related by $q \leq d - 2$ the material is defined to be a topological semimetal [25]. This implies that in two-dimensional topological semimetals only nodes are possible and in three dimensions either nodes or nodal lines may be found. Also the Fermi surface in an ordinary metal can be seen as a topologically protected nodal space, but because this situation is so ordinary, the case $q = d - 1$ has been explicitly ruled out in the definition.

The topological order of the nodal space is defined by its own topological invariant. In many cases this invariant is again the Chern number. We see from Eq. (10) that the nodes act as singularities in the Berry curvature flux. Hence, due to Gauss' law, an integral over a manifold surrounding the singularity gives a non-zero flux and then a finite Chern number. In this context the Chern number is often called the winding number. So the gapped system derived from the surrounding submanifold has a non-trivial topological order, which explains why this submanifold can be seen as a topological insulator in the definition of topological semimetal. Due to the presence of bulk topological insulators, also the topological semimetals possess gapless surface states. Below we present an explicit example in the case of rhombohedral graphite.

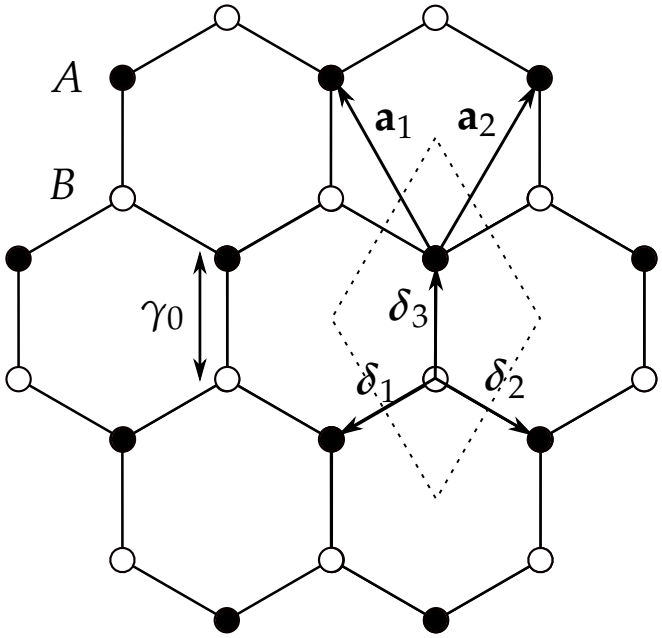

Figure 2: Tight-binding model of graphene lattice. The black balls denote atoms in sublattice A and white balls are atoms in sublattice B. The unit cell is marked with dashed line. Vectors $\boldsymbol{\delta}_i$ connect an atom to three nearest neighbors and vectors $\mathbf{a}_i$ are sublattice vectors. Nearest-neighbor hopping parameter is denoted by γ_0.

3 Graphene

Graphite, used for example in pencils, is the most common form of carbon found in the nature. Take a single-atom-thick layer of it and you will have graphene. In graphene carbon atoms form a honeycomb-like lattice and it can thus be considered as a two-dimensional crystal. This kind of a hexagonal lattice has several interesting properties like remarkably high thermal and electric conductivity. In this section we calculate the linear dispersion of graphene from the tight-binding model in the low-energy limit. This model is quite generic and can be used to describe any hexagonal lattice where the nearest neighbour hopping is dominant. We also discuss the topological properties of the dispersion and study the case of a broken sublattice symmetry. The calculations follow closely the section *Graphene* in Tero Heikkilä's book *The Physics of Nanoelectronics* [9, p. 183].

3.1 Tight-binding model and Dirac fermions

Since hexagonal lattice is not a real Bravais-lattice, we first divide it into two triangular sublattices denoted by A and B (see figure 2). The unit cell of graphene contains then two identical carbon atoms. The sublattices have lattice vectors

$$\mathbf{a}_{1,2} = \mp\frac{\sqrt{3}a}{2}\hat{e}_x + \frac{3a}{2}\hat{e}_y. \tag{14}$$

As a first approximation we include only the nearest-neighbour interaction. Thus every atom A is connected to three B atoms and vice versa. The vectors connecting the site to its nearest neighbours are

$$\boldsymbol{\delta}_1 = -\frac{\sqrt{3}a}{2}\hat{e}_x - \frac{a}{2}\hat{e}_y, \quad \boldsymbol{\delta}_2 = \frac{\sqrt{3}a}{2}\hat{e}_x - \frac{a}{2}\hat{e}_y \quad \text{and} \quad \boldsymbol{\delta}_3 = a\hat{e}_y. \tag{15}$$

Above $a = 1.42\,\text{Å}$ is the distance between the carbon atoms. If the interaction strength is described with a hopping energy γ_0, the tight-binding Hamiltonian of graphene is

$$H = -\gamma_0 \sum_{\mathbf{R}\in A} \psi(\mathbf{R})^\dagger \left[\psi(\mathbf{R}+\boldsymbol{\delta}_1) + \psi(\mathbf{R}+\boldsymbol{\delta}_2) + \psi(\mathbf{R}+\boldsymbol{\delta}_3)\right] + \text{h.c.}, \tag{16}$$

where h.c. stands for "hermitian conjugate", $\psi(\mathbf{R})^\dagger$ is a second quantized particle-creation operator and $\psi(\mathbf{R})$ is the corresponding annihilation operator. In order to calculate the dispersion relation of graphene, the Hamiltonian must be presented in momentum space. This can be done by performing an inverse Fourier transform on the creation and annihilation operators. Since the wavefunctions have Bloch periodicity on the lattice, the inverse Fourier transform reduces to a discrete sum. If annihilation operators for an electron on site A or B with momentum $\mathbf{k}$ are denoted as $c_{A,\mathbf{k}}$ or $c_{B,\mathbf{k}}$, we get

$$\psi(\mathbf{R}) \equiv \frac{1}{\sqrt{N}}\sum_{\mathbf{k}} e^{-i\mathbf{k}\cdot\mathbf{R}} c_{A,\mathbf{k}} \quad \text{and} \quad \psi(\mathbf{R}+\boldsymbol{\delta}_3) \equiv \frac{1}{\sqrt{N}}\sum_{\mathbf{k}} e^{-i\mathbf{k}\cdot\mathbf{R}} c_{B,\mathbf{k}}\,. \tag{17}$$

Substituting this into Hamiltonian (16) gives for example for the first term

$$\begin{aligned}
&\sum_{\mathbf{R}} \psi(\mathbf{R})^\dagger \psi(\mathbf{R}+\boldsymbol{\delta}_1) = \sum_{\mathbf{R}} \psi(\mathbf{R})^\dagger \psi(\mathbf{R}-\mathbf{a}_2+\boldsymbol{\delta}_3) \\
=&\frac{1}{N}\sum_{\mathbf{R}}\sum_{\mathbf{k},\mathbf{k}'} e^{i\mathbf{k}\cdot\mathbf{R}} c^\dagger_{A,\mathbf{k}} e^{-i\mathbf{k}'\cdot\mathbf{R}} e^{i\mathbf{k}'\cdot\mathbf{a}_2} c_{B,\mathbf{k}'} = \sum_{\mathbf{k},\mathbf{k}'}\frac{1}{N}\sum_{\mathbf{R}} e^{i(\mathbf{k}-\mathbf{k}')\cdot\mathbf{R}} e^{i\mathbf{k}'\cdot\mathbf{a}_2} c^\dagger_{A,\mathbf{k}} c_{B,\mathbf{k}'} \\
=&\sum_{\mathbf{k}} e^{i\mathbf{k}\cdot\mathbf{a}_2} c^\dagger_{A,\mathbf{k}} c_{B,\mathbf{k}}\ ,
\end{aligned} \tag{18}$$

where I used

$$\frac{1}{N}\sum_{\mathbf{R}} e^{i(\mathbf{k}-\mathbf{k}')\cdot\mathbf{R}} = \delta_{\mathbf{k},\mathbf{k}'}. \tag{19}$$

Similarly one can deal with the other terms of the Hamiltonian by interchanging $\vec{a}_2 \leftrightarrow \vec{a}_1$ for the second term and setting $\vec{a}_2 \to 0$ for the third term in Eq. (18). Finally the tight-binding Hamiltonian in momentum space reads

$$\begin{aligned} H &= -\gamma_0 \sum_{\mathbf{k}} \left(1 + e^{i\mathbf{k}\cdot\mathbf{a}_1} + e^{i\mathbf{k}\cdot\mathbf{a}_2}\right) c^\dagger_{A,\mathbf{k}} c_{B,\mathbf{k}} + \text{h.c.} \\ &\equiv -\gamma_0 \sum_{\mathbf{k}} \gamma_{\mathbf{k}} c^\dagger_{A,\mathbf{k}} c_{B,\mathbf{k}} + \text{h.c.} \end{aligned} \tag{20}$$

The additional quantum number, the sublattice index A or B, can be regarded as a *pseudospin* of the wavefunction. Therefore it is natural to present the Hamiltonian in the basis of pseudospinors $(c_{A,\mathbf{k}}, c_{B,\mathbf{k}})^T$. Equation (20) is then in a matrix form

$$H = -\gamma_0 \sum_{\mathbf{k}} \begin{pmatrix} 0 & \gamma_{\mathbf{k}} \\ \gamma^*_{\mathbf{k}} & 0 \end{pmatrix}. \tag{21}$$

One can easily calculate the eigenenergies of the Hamiltonian. They are

$$\epsilon_{\mathbf{k}} = \pm\gamma_0 |\gamma_{\mathbf{k}}| = \pm\gamma_0 \sqrt{3 + 2\cos(\sqrt{3}k_x a) + 4\cos(\frac{3k_y a}{2})\cos(\frac{\sqrt{3}k_x a}{2})}. \tag{22}$$

This full dispersion relation of graphene is plotted in figure 3. As can be seen from the picture, the dispersion has several points where $\epsilon_{\mathbf{k}} = 0$. These band touchings are called *Dirac points* and they are all located at the corners of the first Brillouin zone. Due to the periodicity of the reciprocal lattice, only two of the points are non-equivalent (others can be connected to one of these with a linear combination of the reciprocal lattice vectors $\mathbf{G} = n\mathbf{b}_1 + m\mathbf{b}_2$ with n,m integers). The reciprocal lattice vectors are

$$\mathbf{b}_{1,2} = \frac{2\pi}{3a}\left(\mp\sqrt{3}\hat{e}_x + \hat{e}_y\right) \tag{23}$$

and the non-equivalent Dirac points

$$\mathbf{K} = (\mathbf{b}_2 - \mathbf{b}_1)/3 = \frac{4\pi}{3\sqrt{3}a}\hat{e}_x \quad \text{and} \tag{24}$$

$$\mathbf{K}' = (\mathbf{b}_1 - \mathbf{b}_2)/3 = -\frac{4\pi}{3\sqrt{3}a}\hat{e}_x = -\mathbf{K}. \tag{25}$$

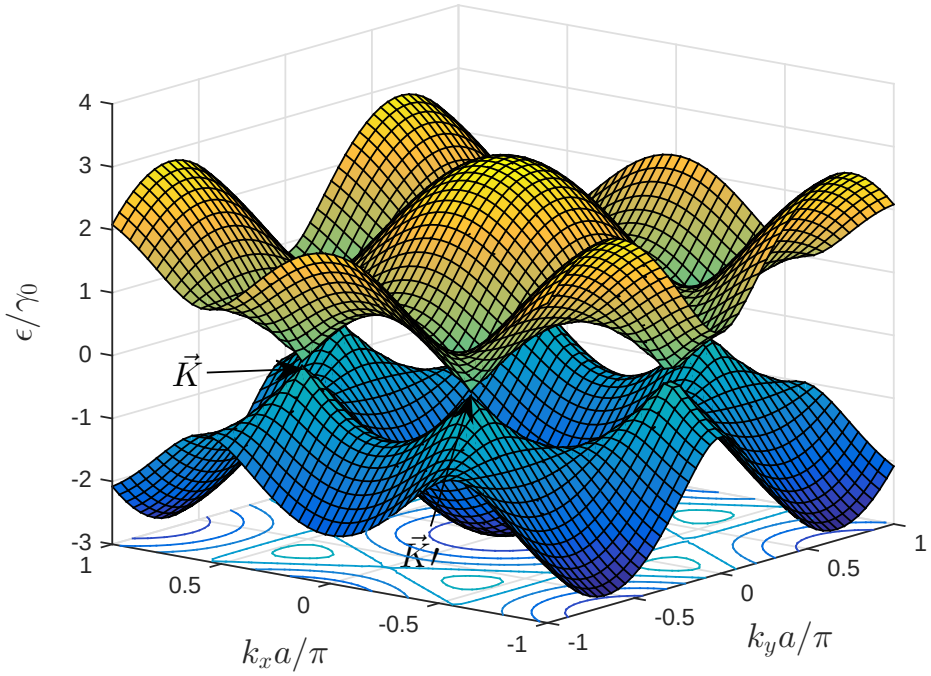

Figure 3: The full dispersion of graphene. The non-equivalent Dirac points are located in the corners of Brillouin zone and are called **K** and **K**′.

Since we are interested in the low-energy limit, we focus on the solutions near these points and make a linear approximation for the Hamiltonian. Small vectors **k** cannot couple the points **K** and **K**′. Therefore the Schrödinger equations near them separate and we may calculate the Hamiltonian around one valley at a time. Near point **K** we have

$$\begin{aligned}\gamma_{\mathbf{k}} &\approx \gamma(\mathbf{K}) + \frac{\mathrm{d}\gamma_{\mathbf{k}}}{\mathrm{d}k}(\mathbf{K})(\mathbf{K}-\mathbf{k}) \\ &= 1 + e^{i\mathbf{K}\cdot\mathbf{a}_1} + e^{i\mathbf{K}\cdot\mathbf{a}_2} + \left(i\mathbf{a}_1 e^{i\mathbf{K}\cdot\mathbf{a}_1} + i\mathbf{a}_2 e^{i\mathbf{K}\cdot\mathbf{a}_2}\right)\cdot(\mathbf{K}-\mathbf{k}).\end{aligned}$$

Let us translate the coordinate system such that $(\mathbf{K}-\mathbf{k}) \to \mathbf{k}$, assuming $|\mathbf{k}| \ll \hbar/a$. With some algebra the equation above comes to a form

$$\gamma_{\mathbf{k}} \approx \frac{3a}{2}(\hat{e}_x - i\hat{e}_y)\mathbf{k} = \frac{3a}{2}\cdot(k_x - ik_y). \tag{26}$$

Respectively near the point **K**′ we get

$$\gamma_{\mathbf{k}} \approx \frac{3a}{2}(-k_x - ik_y). \tag{27}$$

Thus the low-energy Hamiltonian is

$$H \approx \hbar v_F \begin{pmatrix} 0 & \pm k_x - ik_y \\ \pm k_x + ik_y & 0 \end{pmatrix} = \hbar v_F(\pm k_x\sigma_x + k_y\sigma_y) \tag{28}$$

where the different signs correspond to different valleys and $v_F = 3\gamma_0 a/(2\hbar)$ is the Fermi velocity at the Dirac point. The symbols σ_x and σ_y denote the standard Pauli matrices. One notices that replacing the Fermi velocity with speed of light gives exactly the 2-dimensional Dirac Hamiltonian for massless fermions. The dispersion relation is now linear:

$$\epsilon_{\mathbf{k}} \approx \hbar v_F |\mathbf{k}|. \tag{29}$$

The linear dispersion gives rise to many characteristic properties of graphene. Especially, as shown in the next section, the Dirac points are protected by symmetry and topology. The main factors behind the linear dispersion are the honeycomb lattice, *A*–*B*-symmetry and the presence of time reversal symmetry. If one of them is removed, the topological protection of graphene is destroyed. Also this is demonstrated in the section below.

3.2 Stability of Dirac points

In this subsection we see that there are two symmetries in graphene that protect the gapless Dirac points: the time reversal and inversion symmetries. They are enough to make the Dirac points locally stable, though not globally. To examine the symmetries it is necessary to write the linearized Hamiltonian (28) in the original coordinates where

$$H(\mathbf{K} + \mathbf{k}) = k_x\sigma_x + k_y\sigma_y \tag{30}$$

$$H(\mathbf{K}' + \mathbf{k}) = H(-\mathbf{K} + \mathbf{k}) = -k_x\sigma_x + k_y\sigma_y. \tag{31}$$

Let us first consider the symmetry under time reversal that leaves the spatial quantities unchanged and takes $\mathbf{k} \to -\mathbf{k}$. For a spinless fermion Bloch Hamiltonian $H(\mathbf{k})$ the time reversal symmetry requires [2]

$$H(\mathbf{k})^* = H(-\mathbf{k}). \tag{32}$$

We see that our Hamiltonian has this property:

$$H(\mathbf{K} + \mathbf{k})^* = k_x\sigma_x - k_y\sigma_y = H(-\mathbf{K} - \mathbf{k}).$$

If the system obeys inversion symmetry it has the property $H(\mathbf{x}) = H(-\mathbf{x})$. In the hexagonal lattice geometry this symmetry is in the momentum space

$$H(\mathbf{k}) = \sigma_x H(-\mathbf{k})\sigma_x. \tag{33}$$

Again this requirement is fulfilled, since

$$\begin{aligned}\sigma_x H(-\mathbf{K} - \mathbf{k})\sigma_x &= \sigma_x k_x \sigma_x^2 - \sigma_x k_y \sigma_y \sigma_x = k_x\sigma_x - \sigma_x k_y \sigma_x \sigma_y + 2i\sigma_x\sigma_z k_y \\ &= k_x\sigma_x + k_y\sigma_y = H(\mathbf{K} + \mathbf{k}).\end{aligned}$$

Above I used the properties of the Pauli spin matrices.

Next we see how these symmetries together prevent the gap opening. Consider a small perturbation $H_p = \boldsymbol{\alpha} \cdot \boldsymbol{\sigma}$, where $\boldsymbol{\sigma} = (\sigma_x,\sigma_y,\sigma_z)$ and $\boldsymbol{\alpha}$ is a real vector. Since the Pauli spin matrices form a basis in the space of complex 2×2-matrices, this is a general form up to the term proportional to the identity matrix, that is only a trivial shift of the energy level. In units where $\hbar = v_F = 1$ the energy states of the perturbed graphene Hamiltonian $H + H_p$ are

$$\epsilon = \pm\sqrt{(k_x + \alpha_x)^2 + (k_y + \alpha_y)^2 + \alpha_z^2}. \tag{34}$$

We see that the energy is minimized at $(k_x,k_y) = (-\alpha_x, -\alpha_y)$, where $\epsilon = \pm|\alpha_z|$. So there is a gap of $2|\alpha_z|$ in the dispersion that is caused by the term proportional to σ_z whereas small perturbations proportional to σ_x and σ_y only shift the positions of the Dirac points. Indeed, if the time reversal and inversion symmetries are simultaneously required, we get a constraint

$$H(\mathbf{k}) = \sigma_x H(-\mathbf{k})\sigma_x = H^*(-\mathbf{k}) \rightarrow H(\mathbf{k}) = \sigma_x H^*(\mathbf{k})\sigma_x. \tag{35}$$

Then, if the perturbation H_p respects these symmetries, we get for $H + H_p$

$$\begin{aligned}
&(k_x + \alpha_x)\sigma_x + (k_y + \alpha_y)\sigma_y + \alpha_z\sigma_z \\
=&\sigma_x((k_x + \alpha_x)\sigma_x + (k_y + \alpha_y)\sigma_y + \alpha_z\sigma_z)^*\sigma_x \\
=&\sigma_x(k_x + \alpha_x)\sigma_x^2 - \sigma_x(k_y + \alpha_y)\sigma_y\sigma_x + \sigma_x\alpha_z\sigma_z\sigma_x \\
=&(k_x + \alpha_x)\sigma_x + (k_y + \alpha_y)\sigma_y - \alpha_z\sigma_z.
\end{aligned}$$

Thus

$$\alpha_z = -\alpha_z = 0 \tag{36}$$

and the Dirac points are protected by symmetry.

However, if the perturbation respects the time reversal and inversion symmetries, i.e., is of the form $(\alpha_x,\alpha_y,0)$ but is not small, it might move the Dirac points into the same spot in the Brillouin zone. Then the Dirac points annihilate each other and vanish. This can be prevented by demanding an extra symmetry called C_3 from the system. C_3 symmetry requires the Hamiltonian to be invariant under rotations of $2\pi/3$ around a hexagon center or around the points A or B. In practice this requires equal hopping parameters for all the nearest-neighbour hoppings. If this is satisfied the Dirac points are also globally protected.

3.3 Staggering potential

In this work our aim is to explore the effect of breaking the sublattice symmetry of the lattice first in graphene and then in multilayer graphene, graphite. This is

done by adding a staggering potential that is a positive constant α on site A and $-\alpha$ on site B. This kind of a potential could be a consequence of an electron-electron interaction in graphene [18]. The Dirac Hamiltonian becomes

$$H_\alpha = \begin{pmatrix} \alpha & \pm k_x - ik_y \\ \pm k_x + ik_y & -\alpha \end{pmatrix} = \pm k_x \sigma_x + k_y \sigma_y + \alpha \sigma_z. \tag{37}$$

We see immediately that the term $\alpha\sigma_z$ opens up a gap in the dispersion according to the previous subsection. A straightforward calculation shows that this extra term preserves the time reversal symmetry but breaks the inversion symmetry of the system. The Hamiltonian (37) has the eigenenergies

$$\epsilon = \pm\sqrt{|\mathbf{k}|^2 + \alpha^2} \tag{38}$$

so clearly the α-term destroys the linear dispersion and produces an energy gap of 2α. The dispersion relation is shown in Fig. 4.

3.4 Topological properties

Among other interesting properties graphene has also a non-trivial topological structure. In the previous section we notice that the degeneracy points of the energy levels act as sources of Berry curvature flux, and this is also the case with graphene. The topological order of the Dirac points can be defined in terms of the Chern number in a similar way as described in the section on topological semimetals, integrating the Berry curvature along a path around the Dirac point. A useful form for the topological invariant describing graphene is [12]

$$C = \frac{1}{4\pi i}\mathrm{Tr}[\oint \mathrm{d}l \sigma_z H^{-1} \nabla_l H]. \tag{39}$$

Above σ_z is a symmetry operator that anticommutes with H and the integral is over a closed circle in the 2D momentum space. Now if point $\mathbf{K}$ is inside the circle, the Chern number is $C(\mathbf{K}) = 1$ and around $\mathbf{K}'$ the winding number is $C(\mathbf{K}') = -1$ [10]. If the path encloses neither of the Dirac points, the Chern number equals zero. The non-zero topological order implies that the Dirac points are not only protected by symmetry but also by topology. However, if the symmetry of the graphene sheet is broken such that the Hamiltonian no longer anticommutes with the symmetry operator σ_z, a gap opens and the topological protection of the Dirac points vanishes. Below we see that the topological properties of graphene may be transferred also to multilayer graphene. Different stackings lead to different kinds of topological properties in the resulting 3D topological media.

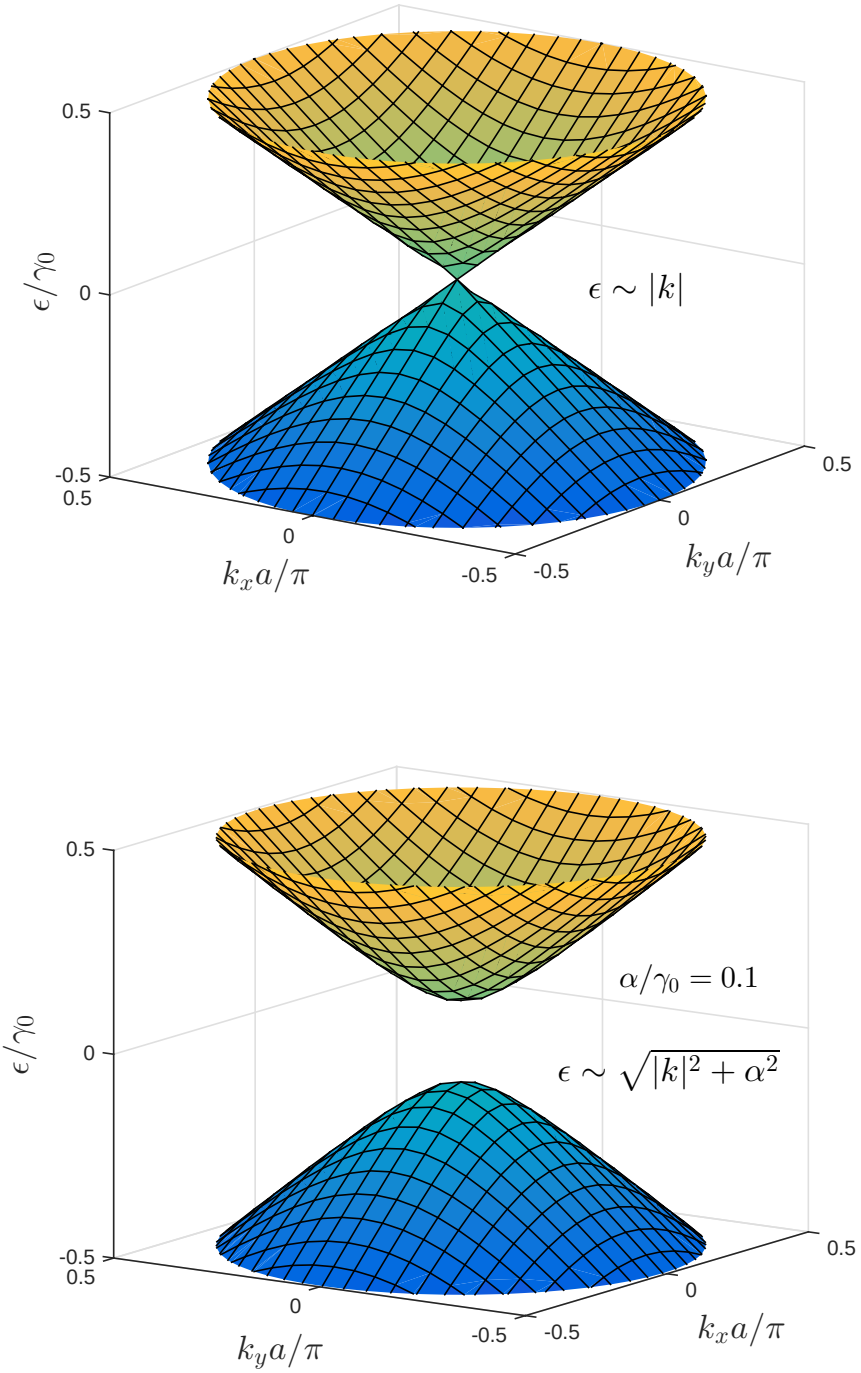

Figure 4: The upper picture presents the linear dispersion (Eq. (29)) around a Dirac point. Below there are the low energy states of graphene with a staggering potential $\alpha = 0.1$ (Eq. (38)). The on-site potential has broken the topological protection of the Dirac point and opened up a gap.

4 Graphite

Although the main focus in condensed matter physics research has for a while been on graphene, also multilayer graphene, graphite, has many newly found interesting properties. There is, however, not an unambiguous way to stack the graphene layers on top of each other and the dispersion relation of graphite depends critically on the stacking. The most common stacking found in the nature is called Bernal or AB stacking where a B atom of the second layer is placed above an A atom of the first layer. The atom A of the second layer is above a center of a hexagon. The third layer is again in the same position as the first layer, so above the atom B of layer two is an atom A of the third layer. The strongest hoppings between the nearest atoms from the successive layers form then a straight line. A recent study shows that Bernal graphite possesses several topological invariants [11]. Studying the Bernal graphite could be a wide subject of its own, but in this work the Bernal graphite is not discussed further.

Another form of stacking is called rhombohedral or ABC stacking. It is still found in nature although not as commonly as Bernal stacking. In rhombohedral graphite every layer is shifted a little with respect to the one below always into the same direction. On top of B atom there is an atom A and above that there is a center of a hexagon. The center of the hexagon is then followed by an atom from sublattice B and so on. The situation is shown in figure 5. Since every layer is oriented in the same way with respect to its neighbours, the unit cell of rhombohedral graphite has atoms only from a single layer. In this work we concentrate on studying rhombohedral graphite because of the exotic dispersion, *flat band*, of the surface states. This may cause for example superconductivity with critical temperature even at room temperature, as we show below. Analogously with the treatment of graphene in the previous section we add a staggering potential $\alpha\sigma_z$ onto the lattice. We begin with describing the tight-binding Hamiltonian of rhombohedral graphite following Ref. [16].

4.1 Tight-binding Hamiltonian of rhombohedral graphite

Apart from the nearest neighbour hopping γ_0 there is now interaction between the graphene layers. In our model only hoppings between neighbouring layers are included. The three most relevant hoppings connecting the layers are shown in Fig. 5. The strongest interlayer hopping that determines the energy scale of the dispersion is called γ_1. It couples an atom A from layer n (A_n) to an atom B from layer $n+1$ (B_{n+1}). Respectively we call the hopping between B_n and A_{n+1} as γ_3 and between $A_n(B_n)$ and $A_{n+1}(B_{n+1})$ as γ_4. The effect of other interlayer hoppings is negligible. We use values $\gamma_0 = 3.16\,\text{eV}$, $\gamma_1 = 0.39\,\text{eV}$, $\gamma_3 = 0.315\,\text{eV}$ and $\gamma_4 = 0.044\,\text{eV}$ for the constants according to [3]. The hopping between the

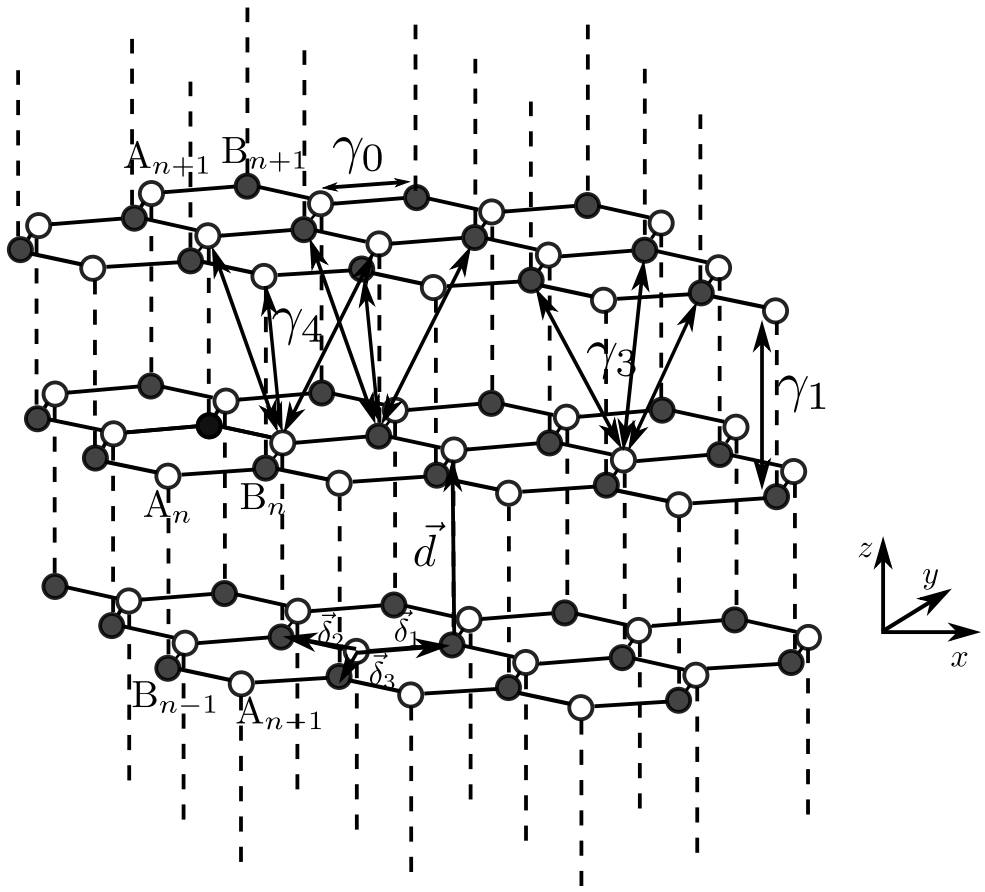

Figure 5: Tight binding model of rhombohedral graphite. The layers are numbered from bottom to top. The lattice hopping and lattice vectors in plane are the same as for a single graphene layer. γ_1, γ_3 and γ_4 are the hoppings between the layers. The picture is from article [16].

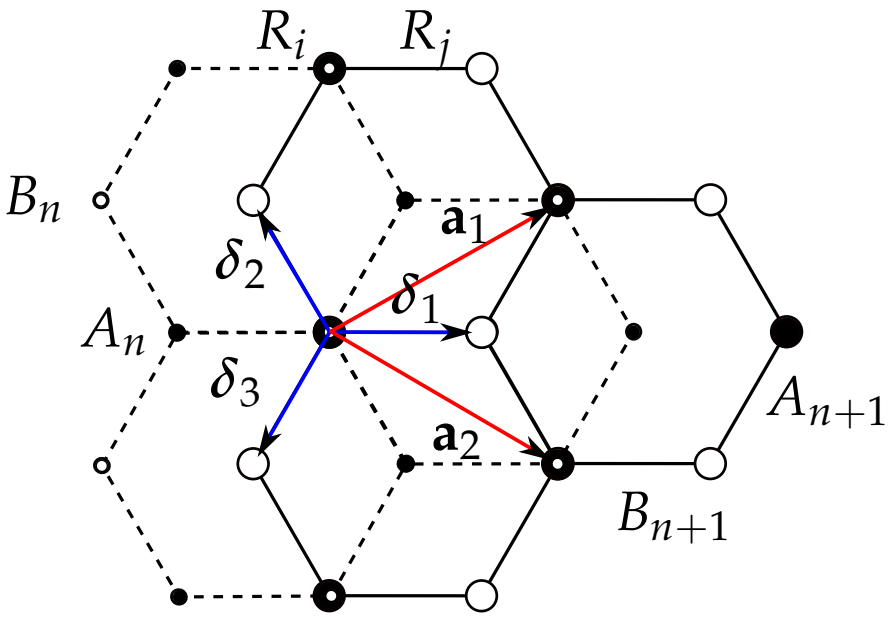

Figure 6: Within the 2D graphene layer the vectors connecting the nearest neighbours are denoted by $\delta_i, i = 1,2,3$. The vectors $\mathbf{a}_1$ and $\mathbf{a}_1$ are the sublattice vectors. The geometry is the same as above with graphene except for a rotation of the layer. The graphene layers are shifted relative to each other such that the B atom of a layer $n+1$ is on top of the hexagon of the layer n below.

next-nearest neighbours within the lattice is measured to be $\gamma_2 = -0.02\,\text{eV}$ so we can neglect it as we do above with graphene. These hoppings are actually obtained for the Bernal graphite and the exact values depend on that which hoppings are included in the model. They are, however, of the right order and produce then a good model of the interactions. One notices immediately that the coupling between the layers is only a tenth of the one inside the layer. So the layers are easy to detach from each other, but breaking a single layer is significantly harder. This is the reason why graphite can be used in pencils.

The tight-binding Hamiltonian can be divided into four parts depending on the different hoppings:

$$H = \sum_{l=0}^{4} H^{(l)} \tag{40}$$

with

$$H^{(0)} = -\gamma_0 \sum_{n=1}^{N} \sum_{\mathbf{R}_{i,n}} \sum_{j=1,2,3} [\psi_n^{A\dagger}(\mathbf{R}_{i,n})\psi_n^B(\mathbf{R}_{i,n} + \delta_j) + \text{h.c.}]$$

$$H^{(1)} = -\gamma_1 \sum_{n=1}^{N-1} \sum_{\mathbf{R}_{i,n}} [\psi_n^{B\dagger}(\mathbf{R}_{i,n} + \delta_1)\psi_{n+1}^A(\mathbf{R}_{i,n} + \mathbf{d} + \delta_1) + \text{h.c.}]$$

$$H^{(3)} = -\gamma_3 \sum_{n=1}^{N-1} \sum_{\mathbf{R}_{i,n}} \sum_{j=1,2,3} [\psi_n^{A\dagger}(\mathbf{R}_{i,n})\psi_{n+1}^B(\mathbf{R}_{i,n} + \mathbf{d} - \delta_j) + \text{h.c.}]$$

$$\begin{aligned} H^{(4)} = -\gamma_4 \sum_{n=1}^{N-1} \sum_{\mathbf{R}_{i,n}} \sum_{j=1,2,3} & [\psi_n^{A\dagger}(\mathbf{R}_{i,n})\psi_{n+1}^A(\mathbf{R}_{i,n} + \mathbf{d} + \delta_j) \\ & -\psi_n^{B\dagger}(\mathbf{R}_{i,n} + \delta_1)\psi_{n+1}^B(\mathbf{R}_{i,n} + \mathbf{d} + \delta_1 + \delta_j) + \text{h.c.}], \end{aligned} \tag{41}$$

where N is the number of graphene layers and the $\mathbf{R}_i$ sum goes over all the A sites in the layer. Here the coordinate system is chosen to be slightly different to that above with graphene as one can see from figure 6. The unit cell vectors of the sublattice are now

$$\mathbf{a}_1 = \frac{3a}{2}\hat{e}_x + \frac{\sqrt{3}a}{2}\hat{e}_y, \quad \mathbf{a}_2 = \frac{3a}{2}\hat{e}_x - \frac{\sqrt{3}a}{2}\hat{e}_y, \quad \mathbf{a}_3 = \mathbf{d} + \delta_1 \tag{42}$$

and the vectors connecting nearest neighbours within a plane are

$$\delta_1 = a\hat{e}_x, \quad \delta_2 = -\frac{a}{2}\hat{e}_x + \frac{\sqrt{3}a}{2}\hat{e}_y, \quad \delta_3 = -\frac{a}{2}\hat{e}_x - \frac{\sqrt{3}a}{2}\hat{e}_y. \tag{43}$$

Since a single graphene sheet has Dirac points at $\mathbf{K}$ and $\mathbf{K}'$ and linear dispersion around them, it is a good guess that something similarly interesting happens also for graphite dispersion around these points. Therefore we perform again an inverse Fourier transform on the tight-binding Hamiltonian and expand it around points $\mathbf{K}$ and $\mathbf{K}'$. In this coordinate system these points are

$$\mathbf{K} = \frac{2\pi}{3a}\hat{e}_x + \frac{2\pi}{3\sqrt{3}a}\hat{e}_y, \quad \mathbf{K} = \frac{2\pi}{3a}\hat{e}_x - \frac{2\pi}{3\sqrt{3}a}\hat{e}_y \tag{44}$$

and the inverse Fourier transform is

$$\psi_n^A(\mathbf{R}_i) = \frac{1}{\sqrt{L}} \sum_{\mathbf{p}} e^{i(\mathbf{K}+\mathbf{p}/\hbar)\cdot\mathbf{R}_i} \psi_n^A(\mathbf{p}), \tag{45}$$

$$\psi_n^B(\mathbf{R}_i + \delta_j) = \frac{1}{\sqrt{L}} \sum_{\mathbf{p}'} e^{i(\mathbf{K}+\mathbf{p}'/\hbar)\cdot(\mathbf{R}_i+\delta_j)} \psi_n^B(\mathbf{p}') \tag{46}$$

where L is the number of unit cells in a given layer and $|\mathbf{p}|, |\mathbf{p}'| \ll \hbar/a$. Again the small momenta -approximation leaves the valleys $\mathbf{K}$ and $\mathbf{K}'$ separate. Let us concentrate on the valley $\mathbf{K}$ first.

The inverse Fourier transforms for $H^{(0)}$ go analogously with the transform of the graphene Hamiltonian, except now we have an extra global phase factor $e^{i\pi/6}$ due to the rotation of the coordinate system of an angle $\pi/6$. Substituting Eqs. (45) and (46) into the definition of $H^{(0)}$ gives

$$H^{(0)} = -\frac{\gamma_0}{L}\sum_{n=1}^{N}\sum_{\mathbf{R}_i}\sum_{\mathbf{p},\mathbf{p}'} e^{(\mathbf{K}+\mathbf{p}'/\hbar-\mathbf{K}-\mathbf{p}/\hbar)\cdot\mathbf{R}}\sum_{j=1,2,3} e^{i(\mathbf{K}+\mathbf{p}'/\hbar)\cdot\boldsymbol{\delta}_j}\psi_n^{A\dagger}(\mathbf{p})\psi_n^{B}(\mathbf{p}') + \text{h.c.} \tag{47}$$

Using definition (19) for the delta function simplifies the equation to

$$H^{(0)} = -\gamma_0\sum_{n=1}^{N}\sum_{\mathbf{p}}\gamma_{\mathbf{p}}^{(0)}\psi_n^{A\dagger}(\mathbf{p})\psi_n^{B}(\mathbf{p}) + \text{h.c.}\,, \tag{48}$$

where

$$\gamma_{\mathbf{p}}^{(0)} = \sum_{j=1,2,3} e^{i(\mathbf{K}+\mathbf{p}/\hbar)\cdot\boldsymbol{\delta}_j}. \tag{49}$$

To calculate this we need the dot products

$$\mathbf{K}\cdot\boldsymbol{\delta}_1 = \frac{2\pi}{3}, \quad \mathbf{K}\cdot\boldsymbol{\delta}_2 = 0 \quad \text{and} \quad \mathbf{K}\cdot\boldsymbol{\delta}_3 = -\frac{2\pi}{3}. \tag{50}$$

The equation to linearize is then

$$\begin{aligned}
\gamma_{\mathbf{p}}^{(0)} &= e^{i2\pi/3}e^{(i/\hbar)\mathbf{p}\cdot\boldsymbol{\delta}_1} + e^{(i/\hbar)\mathbf{p}\cdot\boldsymbol{\delta}_2} + e^{-i2\pi/3}e^{(i/\hbar)\mathbf{p}\cdot\boldsymbol{\delta}_3} \\
&\approx 0 + i\left(e^{i2\pi/3}\boldsymbol{\delta}_1 + \boldsymbol{\delta}_2 + e^{-i2\pi/3}\boldsymbol{\delta}_3\right)\cdot\mathbf{p} \\
&= -\left(\frac{\sqrt{3}}{2} + \frac{i}{2}\right)\cdot\frac{3a}{2\hbar}(p_x - ip_y) \\
&= e^{i\pi/6}\left[-\frac{3a}{2\hbar}(p_x - ip_y)\right],
\end{aligned}$$

where I used

$$e^{\pm i2\pi/3} = -\frac{1}{2} \pm i\frac{\sqrt{3}}{2}.$$

The transformation into momentum space goes analogously for other terms of the Hamiltonian. For example

$$H^{(1)} = -\gamma_1\sum_{n=1}^{N-1}\sum_{\mathbf{p}}\gamma_{\mathbf{p}}^{(1)}\psi_{n+1}^{B\dagger}(\mathbf{p})\psi_n^{A}(\mathbf{p}) + \text{h.c.} \tag{51}$$

with

$$\gamma_{\mathbf{p}}^{(1)} = 1 = e^{i\pi/6} \cdot e^{-i\pi/6}. \tag{52}$$

We present the Hamiltonian again in the basis of pseudo-spinors. They are now defined as

$$\hat{\psi}_n = \begin{pmatrix} \psi_n^A \\ e^{i\pi/6}\psi_n^B \end{pmatrix}, \quad \hat{\psi}_n{}^\dagger = (\psi_n^{A\dagger}, e^{-i\pi/6}\psi_n^{B\dagger}) \tag{53}$$

which gives the $2N \times 2N$-Hamiltonian of the rhombohedral graphite (neglecting the global phase shift $e^{i\pi/6}$)

$$H_{\mathbf{K}} = \sum_{\mathbf{p}} \sum_{n,m=1}^{N} \hat{\psi}_n^\dagger(\mathbf{p}) \hat{H}_{nm}(\mathbf{K},\mathbf{p}) \hat{\psi}_m(\mathbf{p}), \tag{54}$$

$$\hat{H}_{nm}(\mathbf{K},\mathbf{p}) = \sum_{l=0}^{4} \hat{H}_{nm}^{(l)}(\mathbf{K},\mathbf{p}), \tag{55}$$

where

$$\begin{aligned}
\hat{H}_{nm}^{(0)}(\mathbf{K},\mathbf{p}) &= v_F(\hat{\boldsymbol{\sigma}} \cdot \mathbf{p} + \alpha\hat{\sigma}_z)\delta_{mn} \\
\hat{H}_{nm}^{(1)}(\mathbf{K},\mathbf{p}) &= -\gamma_1 \left[e^{-i\pi/6}\sigma_+\delta_{n,m+1} + e^{i\pi/6}\sigma_-\delta_{n,m-1} \right] \\
\hat{H}_{nm}^{(3)}(\mathbf{K},\mathbf{p}) &= \frac{\gamma_3}{\gamma_0} v_F \left[e^{-i\pi/3}\sigma_+ p_+ \delta_{n,m-1} + e^{i\pi/3}\sigma_- p_- \delta_{n,m+1} \right] \\
\hat{H}_{nm}^{(4)}(\mathbf{K},\mathbf{p}) &= \frac{\gamma_4}{\gamma_0} v_F \left[e^{i\pi/6} p_- \delta_{n,m-1} + e^{-i\pi/6} p_+ \delta_{n,m+1} \right].
\end{aligned}$$

Here $v_F = 3a\gamma_0/2\hbar$ as above , $\hat{\boldsymbol{\sigma}} = (\sigma_x,\sigma_y)$ is a vector of Pauli matrices in the xy-plane and $\sigma_\pm = \frac{1}{2}(\sigma_x \pm i\sigma_y)$. Similarly we denote $p_\pm = p_x \pm ip_y = pe^{\pm i\phi}$. Here 2α is the on-site energy difference between lattice sites A and B.

4.2 Bulk modes

In the bulk the Schrödinger equation of rhombohedral graphite becomes

$$\sum_m \hat{H}_{nm}(\mathbf{K},\mathbf{p})\hat{\psi}_m(\mathbf{p}) = (\epsilon + \mu)\hat{\psi}_n(\mathbf{p}), \tag{56}$$

where the energy $E = \epsilon + \mu$ consists of interaction energy ϵ and chemical potential μ. From Eq. (55) we can see that most of the terms in the sum above are zero. As mentioned at the beginning of the section, rhombohedral graphite is periodic in the z-direction with the periodicity length of one layer. Since one

row of the Hamiltonian corresponds to one graphene layer, the same periodicity manifests itself also there. Thus we can write

$$\lambda_1 \equiv \hat{H}_{n(n-1)} = -\gamma_1 e^{-i\pi/6}\sigma_+ + \frac{\gamma_3}{\gamma_0} v_F e^{i\pi/3}(\sigma_- p_-) + \frac{\gamma_4}{\gamma_0} v_F e^{-i\pi/6} p_+$$
$$\lambda_2 \equiv \hat{H}_{nn} = v_F(\hat{\boldsymbol{\sigma}} \cdot \mathbf{p} + \alpha\hat{\sigma}_z)$$
$$\lambda_3 \equiv \hat{H}_{n(n+1)} = -\gamma_1 e^{i\pi/6}\sigma_- + \frac{\gamma_3}{\gamma_0} v_F e^{-i\pi/3}(\sigma_+ p_+) + \frac{\gamma_4}{\gamma_0} v_F e^{i\pi/6} p_-$$

for all $n \neq 1,N$ where λ_i are 2×2-matrices. The Schrödinger equation (56) reduces to

$$\sum_m (\lambda_1 \delta_{n,m+1} + \lambda_2 \delta_{n,m} + \lambda_3 \delta_{n,m-1})\hat{\psi}_m(\mathbf{p}) = (\epsilon + \mu)\hat{\psi}_n(\mathbf{p}) \tag{57}$$

At the moment our system is presented partly in momentum space (p_x,p_y-plane) and partly in real space (layer indices n in z-direction). Therefore we perform yet another Fourier inverse transform to replace the indices n,m with a momentum space variable q. Equation (57) reads then

$$\int_q \sum_m (\lambda_1 \delta_{n,m+1} + \lambda_2 \delta_{n,m} + \lambda_3 \delta_{n,m-1}) e^{imqd} \hat{\psi}_q(\mathbf{p}) \mathrm{d}q = \int_q (\epsilon + \mu) e^{inqd} \hat{\psi}_q(\mathbf{p}) \mathrm{d}q$$
$$\Rightarrow \int_q (\lambda_1 e^{-iqd} + \lambda_2 + \lambda_3 e^{iqd}) e^{inqd} \hat{\psi}_q(\mathbf{p}) \mathrm{d}q = \int_q (\epsilon + \mu) e^{inqd} \hat{\psi}_q(\mathbf{p}) \mathrm{d}q.$$

Since this should hold for all n, we can simplify it with the Ansatz

$$\hat{\psi}_q(\mathbf{p}) = \begin{pmatrix} A_1 \\ A_2 e^{i\pi/6} \end{pmatrix} \tag{58}$$

satisfying

$$(\lambda_1 e^{-iqd} + \lambda_2 + \lambda_3 e^{iqd}) \begin{pmatrix} A_1 \\ A_2 e^{i\pi/6} \end{pmatrix} = (\epsilon + \mu) \begin{pmatrix} A_1 \\ A_2 e^{i\pi/6} \end{pmatrix}, \tag{59}$$

where $A_1, A_2 \in \mathbb{C}$ are arbitrary coefficients. Above we have formulated the bulk Hamiltonian

$$H_{bulk} = \lambda_1 e^{-iqd} + \lambda_2 + \lambda_3 e^{iqd}, \tag{60}$$

which is a 2×2-matrix and describes the kinetics in the limit $N \to \infty$. Next we write the Ansatz (59) term by term to get explicit conditions for the eigenener-

gies:

$$\lambda_1 e^{-iqd}\begin{pmatrix} A_1 \\ A_2 e^{i\pi/6}\end{pmatrix} = \begin{pmatrix} e^{-i\pi/6}p_+\dfrac{\gamma_4}{\gamma_0}v_F & -e^{-i\pi/6}\gamma_1 \\ e^{i\pi/3}p_-\dfrac{\gamma_3}{\gamma_0}v_F & e^{-i\pi/6}p_+\dfrac{\gamma_4}{\gamma_0}v_F\end{pmatrix}\begin{pmatrix} A_1 \\ A_2 e^{i\pi/6}\end{pmatrix} e^{-iqd}$$
$$= \begin{pmatrix} A_1 e^{-i\pi/6}p_+\dfrac{\gamma_4}{\gamma_0}v_F - A_2\gamma_1 \\ A_1 e^{i\pi/3}\dfrac{\gamma_3}{\gamma_0}v_F p_- + A_2 p_+\dfrac{\gamma_4}{\gamma_0}v_F\end{pmatrix} e^{-iqd},$$

$$\lambda_2\begin{pmatrix} A_1 \\ A_2 e^{i\pi/6}\end{pmatrix} = \begin{pmatrix} \alpha & v_F p_- \\ v_F p_+ & -\alpha\end{pmatrix}\begin{pmatrix} A_1 \\ A_2 e^{i\pi/6}\end{pmatrix} = \begin{pmatrix} A_1\alpha + A_2 e^{i\pi/6}v_F p_- \\ A_1 v_F p_+ - A_2 e^{i\pi/6}\alpha\end{pmatrix},$$

$$\lambda_3 e^{iqd}\begin{pmatrix} A_1 \\ A_2 e^{i\pi/6}\end{pmatrix} = \begin{pmatrix} e^{i\pi/6}p_-\dfrac{\gamma_4}{\gamma_0}v_F & e^{-i\pi/3}\dfrac{\gamma_3}{\gamma_0}v_F p_+ \\ -e^{i\pi/6}\gamma_1 & e_-^{pi\pi/6}\dfrac{\gamma_4}{\gamma_0}v_F\end{pmatrix}\begin{pmatrix} A_1 \\ A_2 e^{i\pi/6}\end{pmatrix} e^{iqd}$$
$$= \begin{pmatrix} A_1 e^{i\pi/6}p_-\dfrac{\gamma_4}{\gamma_0}v_F + A_2 e^{-i\pi/6}\dfrac{\gamma_3}{\gamma_0}v_F p_+ \\ -A_1 e^{i\pi/6}\gamma_1 + A_2 e^{i\pi/3}p_-\dfrac{\gamma_4}{\gamma_0}v_F\end{pmatrix} e^{iqd},$$

$$\text{and}\quad (\epsilon+\mu)\begin{pmatrix} A_1 \\ A_2 e^{i\pi/6}\end{pmatrix} = \begin{pmatrix} (\epsilon+\mu)A_1 \\ e^{i\pi/6}(\epsilon+\mu)A_2\end{pmatrix}$$

Equation (59) gives then two independent conditions for coefficients A_1 and A_2. Using notations $\phi = \tilde{\phi} + \pi/6$ and $p_\pm = pe^{\pm i\phi}$ we get from the upper row

$$\left[v_F p e^{-i\tilde{\phi}} - \gamma_1 e^{-iqd} + \frac{\gamma_3}{\gamma_0}v_F p e^{i(qd+\tilde{\phi})}\right] A_2$$
$$+ \left[2\frac{\gamma_4}{\gamma_0}v_F p\cos(\tilde{\phi} - qd) - (\epsilon - \alpha + \mu)\right] A_1 = 0$$

and from the lower

$$\left[v_F p e^{i\tilde{\phi}} - \gamma_1 e^{iqd} + \frac{\gamma_3}{\gamma_0}v_F p e^{-i(qd+\tilde{\phi})}\right] A_1$$
$$+ \left[2\frac{\gamma_4}{\gamma_0}v_F p\cos(\tilde{\phi} - qd) - (\epsilon + \alpha + \mu)\right] A_2 = 0.$$

The pair of equations yields the low-energy spectrum in the bulk:

$$\left[\epsilon + \mu - 2\frac{\gamma_4}{\gamma_0}v_F p\cos(\tilde{\phi} - qd)\right]^2 - \alpha^2 = (v_F p)^2 + \gamma_1^2 - 2v_F p\gamma_1\cos(\tilde{\phi} - qd)$$
$$+ \left(\frac{\gamma_3}{\gamma_0}\right)^2 (v_F p)^2 + 2\frac{\gamma_3}{\gamma_0}(v_F p)^2\cos(2\tilde{\phi} + qd) - 2\gamma_1\frac{\gamma_3}{\gamma_0}(v_F p)\cos(2\tilde{\phi} + qd).$$

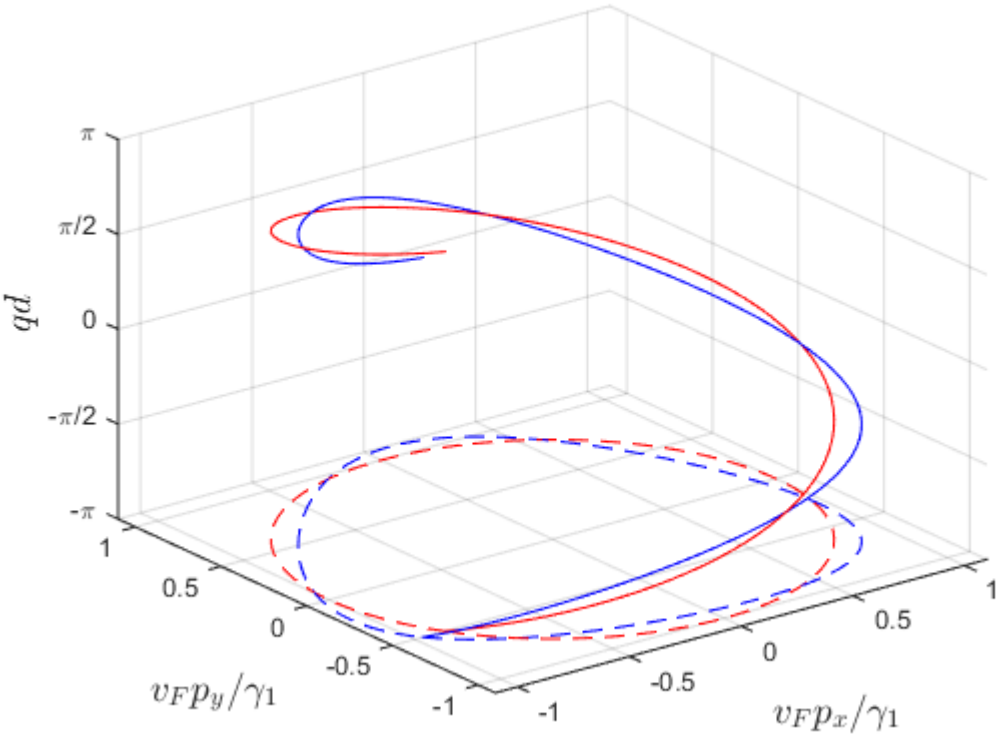

Figure 7: The Fermi line of bulk states for $\alpha = 0$. The red line is corresponds to $\gamma_3 = \gamma_4 = 0$ whereas the blue line shows the Fermi line with $\gamma_4 = 0$, $\gamma_3 \neq 0$. The dashed loops are the projections of the spirals onto the $x - y$-plane

If the weakest interactions γ_3 and γ_4 are neglected and the chemical potential μ is set to zero, the compatibility condition reduces to a Dirac line

$$\epsilon^2 - \alpha^2 = v_F^2 p^2 + \gamma_1^2 - 2 v_F p \gamma_1 \cos(\tilde{\phi} - qd). \tag{61}$$

A real solution for p is obtained only if $|\epsilon| \geq \alpha$. In the limit $\epsilon = \pm\alpha$ the possible values for momenta p,q are on the spiral $v_F p = \gamma_1$, $\tilde{\phi} = qd$. In the case $\alpha = 0$ the spiral is a Fermi line for zero doping $\epsilon = \mu = 0$.

4.3 Rhombohedral graphite as a topological semimetal

Above we obtain that in the bulk the zeros of dispersion form a nodal line, i.e., a 1D nodal space. Since now the difference in the dimensions of the system and the nodal space is $3 - 1 = 2$, graphite is potentially a topological semimetal

according to the definition given above. Next we need to define the topological properties of the nodal line and the surrounding bulk states. Let us study closer the bulk Hamiltonian (60). If we neglect the weakest hopping parameter $\gamma_4 = 0$ and set the staggering potential $\alpha = 0$, the Hamiltonian is

$$H_{bulk} = \begin{pmatrix} 0 & f \\ f^* & 0 \end{pmatrix} \tag{62}$$

with

$$f = p_- - \gamma_1 e^{-iqd} + \frac{\gamma_3}{\gamma_0} v_F p_+ e^{iqd}, \tag{63}$$

where I neglect the global phase factor $e^{i\pi/6}$ and rotate the coordinate system in the $x-y$-plane such that $\tilde{\phi} \to \phi$. In terms of Pauli spin matrices the bulk Hamiltonian can be written as

$$\begin{aligned} H =& p_x\sigma_x + p_y\sigma_y \\ &-(\cos(qd)(\gamma_1 - \gamma_3 p_x) + p_y \sin(qd))\sigma_x \\ &-(\sin(qd)(\gamma_1 + \gamma_3 p_x) + p_y \cos(qd))\sigma_y. \end{aligned}$$

If we now fix the momentum q into z-direction, we get a familiar 2D Hamiltonian. It describes graphene where the position of Dirac points is shifted by a perturbation proportional to σ_x and σ_y. Indeed, it seems that the interesting properties of a single-layer graphene are still present in the bulk of graphite. The nodal line is protected by the topological invariant [13]

$$C(q) = C = \frac{1}{4\pi i}\mathrm{Tr}[\oint \mathrm{d}l \sigma_z H^{-1} \nabla_l H] \tag{64}$$

that coincides with the topological invariant (39) describing graphite for any $q \in [-\pi/d, \pi/d]$. The integral along a loop in (p_x,p_y)-plane around the nodal line gives the winding number $C = 1$. So the Fermi line is robust against perturbations.

Let us then investigate the topological invariant in the direction we ignored above. The former topological invariant can also be defined for a 1D submanifold along q-axis that is parametrized by the transversal momentum $\mathbf{p}_\perp$. Due to periodic boundary conditions, interval $q \in [-\pi/d, \pi/d]$ forms a closed loop in the Brillouin zone. Then for a fixed $\mathbf{p}_\perp$ the topological invariant is

$$C(\mathbf{p}_\perp) = \frac{1}{4\pi i}\mathrm{Tr}[\int_{-\pi/d}^{\pi/d} \mathrm{d}p_z \sigma_z H^{-1} \nabla_{p_z} H]. \tag{65}$$

The integration paths for the invariants $C(q)$ and $C(\mathbf{p}_\perp)$ are illustrated in Fig. 8. If we neglect the hopping γ_3 for a moment, we see that the projection of the

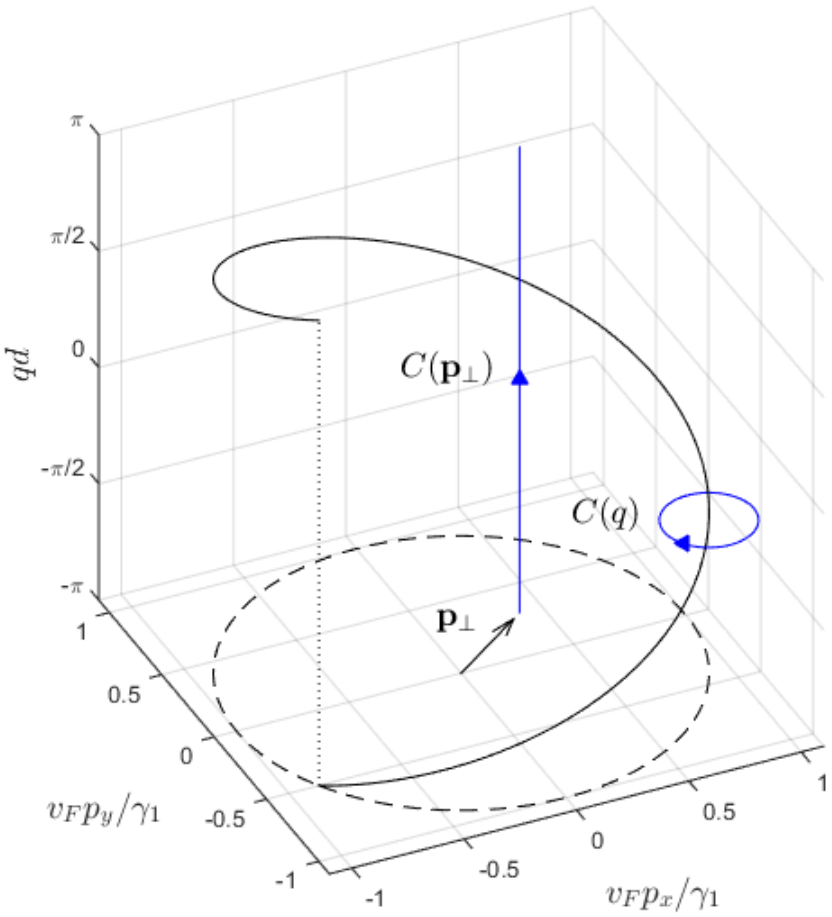

Figure 8: The Fermi spiral of the bulk states. Blue lines are examples of integration paths for invariants $C(q)$ and $C(\mathbf{p}_\perp)$. The transversal momentum $|\mathbf{p}_\perp|$ parametrizes the 1D submanifold parallel to q. Here $\gamma_3 = 0$ and the projection of the spiral is a circle with radius γ_1/v_F.

spiral into $x-y$-plane forms a circle $|\mathbf{p}_\perp| = p = \gamma_1/v_F$. For the transversal momenta either inside or outside the circle the corresponding 1D system parallel to q is fully gapped. According to [13], for $p < \gamma_1/v_F$ the topological invariant (65) is $N(\mathbf{p}_\perp) = 1$ whereas for $p > \gamma_1/v_F$ it is $N(\mathbf{p}_\perp) = 0$. So inside the circle the 1D system parallel to q can be seen as a topological insulator and outside the circle the insulator is topologically trivial. We conclude that the nodal line $p = \gamma_1/v_F$ can be seen as a topologically protected boundary of topological and non-topological insulators and therefore this model of graphite represents a topological semimetal.

The presence of topological insulators defines also the topology of the surface states through the bulk-boundary correspondence. At the surface layer, each point with $p < \gamma_1/v_F$ is a boundary of a 1D topological insulator where the energy must be strictly zero. Together these points form a disc of zero modes, a *flat band*. The existence of the flat band is confirmed by a numerical diagonalization of the Hamiltonian (55). The numerically solved surface states are shown in Fig. 9. Below we also solve the surface state energies analytically including the hopping γ_4.

Let us then restore the hopping γ_3. Does this extra term violate the existence of flat band? The answer is obviously no since γ_3 comes with matrices σ_x and σ_y that anticommute with the symmetry operator σ_z. So even with this extra term the Hamiltonian still fulfils $\{\sigma_z, H\} = 0$. Its presence nevertheless affects the position of the Dirac points in the 2D cross-section and so to the form of the nodal line. Also the projection of the line onto the surface deforms reshaping the flat band as can be seen in Fig. 9.

4.4 Surface states of rhombohedral graphite

Next we find the analytical solution for the Schrödinger equation (56). For simplicity we set $\gamma_3 = 0$ since it does not have an effect on the topological properties of the dispersion, as discussed above, but include the hopping γ_4 and the staggering potential α. The equation to solve is then

$$\begin{aligned}(v_F(\boldsymbol{\sigma}\cdot\mathbf{p}) + \alpha\sigma_z))\hat{\psi}_n(\mathbf{p}) - \gamma_1\left[e^{i\pi/6}\sigma_-\hat{\psi}_{n+1}(\mathbf{p}) + e^{-i\pi/6}\sigma_+\hat{\psi}_{n-1}(\mathbf{p})\right] \\ + \frac{\gamma_4}{\gamma_0}\left[e^{i\pi/6}v_F p_-\hat{\psi}_{n+1}(\mathbf{p}) + e^{-i\pi/6}v_F p_+\hat{\psi}_{n-1}(\mathbf{p})\right] = (\epsilon+\mu)\hat{\psi}_n(\mathbf{p}). \qquad (66)\end{aligned}$$

Let us make an Ansatz

$$\begin{aligned}\hat{\psi}_n(\mathbf{p}) = e^{i(\psi-\pi/6)(n-1-\frac{N}{2})} \\ \times\left[\left(\frac{v_F p}{\gamma_1}\right)^{n-1}\begin{pmatrix}1\\ \zeta_2 e^{i\psi}\end{pmatrix}A_+ + \left(\frac{v_F p}{\gamma_1}\right)^{N-n}\begin{pmatrix}\zeta_1\\ e^{i\psi}\end{pmatrix}A_-\right] \qquad (67)\end{aligned}$$

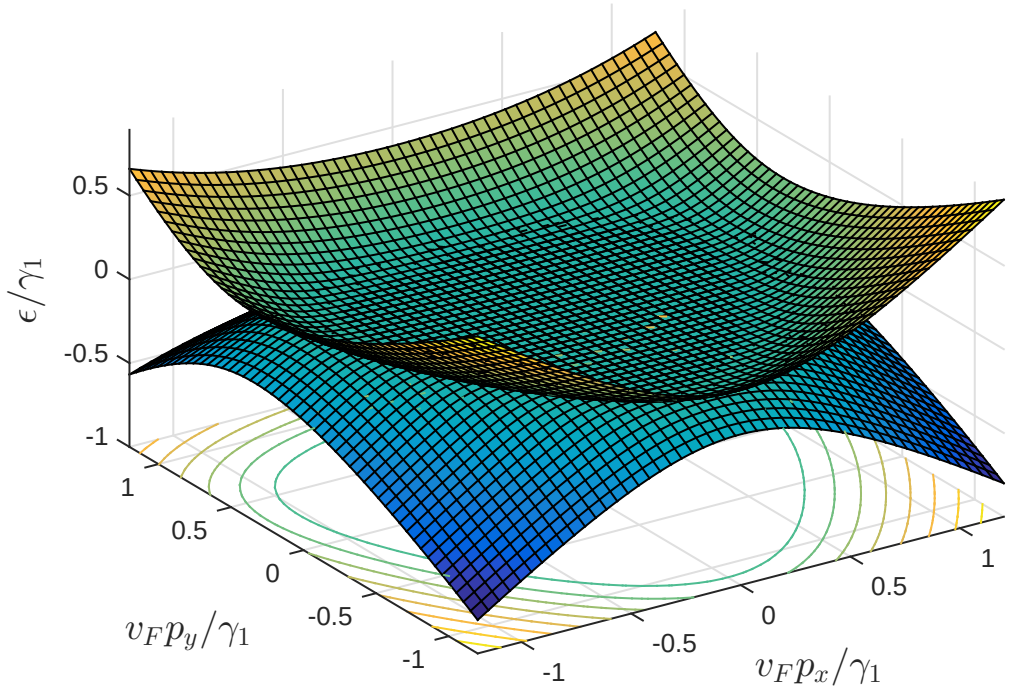

Figure 9: The surface energy states of rhombohedral graphite calculated numerically from the tight-binding Hamiltonian (55). Here the number of layers is $N = 20$. The hopping γ_3 changes the shape of the flat band from a circle into a triangle like area. The effect of γ_4 does not show up on this scale.

where A_-,A_+ are arbitrary coefficients and

$$\begin{aligned}\zeta_{\frac{1}{2}} &= \left(\frac{v_F p}{\gamma_1}\right) \frac{\gamma_1(\epsilon+\mu\pm\alpha) - (\gamma_4/\gamma_0)(v_F^2p^2-\gamma_1^2)}{v_F^2p^2-\gamma_1^2} \\ &\equiv \zeta \pm \tilde{\zeta} \end{aligned} \tag{68}$$

with

$$\tilde{\zeta} = \left(\frac{v_F p}{\gamma_1}\right) \frac{\gamma_1 \alpha}{v_F^2 p^2 - \gamma_1^2}.$$

This corresponds to the Ansatz made in reference [16] for the case $\alpha = 0$. The consistence of the Ansatz is shown in Appendix B. We study next the Schrödinger equation (56) for the surface layers, i.e., for states $\hat{\psi}_1$ and $\hat{\psi}_N$. The terms containing $\hat{\psi}_0$ and $\hat{\psi}_{N+1}$ vanish. Thus Eq. (66) reads for $n = 1$

$$\begin{aligned}\begin{pmatrix} \alpha\psi_1^A + v_F p_- \psi_1^B \\ v_F p_+ \psi_1^A - \alpha \psi_1^B \end{pmatrix} - \gamma_1 e^{i\pi/6} \begin{pmatrix} 0 \\ \psi_2^B \end{pmatrix} + \frac{\gamma_4}{\gamma_0} v_F e^{i\pi/6} v_F p_- \begin{pmatrix} \psi_2^A \\ \psi_2^B \end{pmatrix} \\ = (\epsilon+\mu) \begin{pmatrix} \psi_1^A \\ \psi_1^B \end{pmatrix}. \end{aligned} \tag{69}$$

This determines two independent equations, one including a γ_1-term and one without it. The Ansatz satisfies the equation that contains γ_1 but gives no constraints for A_+ or A_-. We consider then the equation where γ_1 is absent and take the upper row from Eq. (69). After a similar treatment for the case $n = N$ we have two equations:

$$v_F p e^{-i\phi}\psi_1^B + \frac{\gamma_4}{\gamma_0} v_F p e^{-i(\phi-\pi/6)}\psi_2^A = (\epsilon + \mu - \alpha)\psi_1^A \tag{70}$$

$$v_F p e^{i\phi}\psi_N^A + \frac{\gamma_4}{\gamma_0} v_F p e^{i(\phi-\pi/6)}\psi_{N-1}^B = (\epsilon + \mu + \alpha)\psi_N^B, \tag{71}$$

where I used $p_\pm = pe^{\pm i\phi}$. Substitution of Ansatz (67) into Eq. (70) gives

$$\begin{aligned} & v_F p e^{-i\phi} e^{i(\phi-\pi/6)\frac{N}{2}} e^{i\phi} \left[\zeta_2 A_+ + \left(\frac{v_F p}{\gamma_1}\right)^{N-1} A_-\right] \\ + \frac{\gamma_4}{\gamma_0} v_F p e^{-i(\phi-\pi/6)} & e^{i(\phi-\pi/6)(1-\frac{N}{2})} \left[\left(\frac{v_F p}{\gamma_1}\right) A_+ + \left(\frac{v_F p}{\gamma_1}\right)^{N-2} \zeta_1 A_-\right] \\ & = (\epsilon + \mu - \alpha) e^{i(\phi-\pi/6)\frac{N}{2}} \left[A_+ + \left(\frac{v_F p}{\gamma_1}\right)^{N-1} \zeta_1 A_-\right]. \end{aligned} \tag{72}$$

The phase factors cancel out which simplifies the equation a little. The next task is to substitute the definitions of $\zeta_{\frac{1}{2}} = \zeta \pm \tilde{\zeta}$. We also define a new variable

$$\xi_p \equiv \gamma_1 \left(\frac{v_F p}{\gamma_1}\right)^N. \tag{73}$$

Equation (72) becomes

$$(-B + \alpha')A_+ = (-C + \delta - \lambda)A_-, \tag{74}$$

where

$$\begin{aligned} B &\equiv -v_F p\zeta - \frac{\gamma_4}{\gamma_0} v_F p \left(\frac{v_F p}{\gamma_1}\right) + (\epsilon + \mu) = \frac{\gamma_1}{\gamma_1^2 - v_F^2 p^2}\left[\gamma_1(\epsilon + \mu) - 2\frac{\gamma_4}{\gamma_0} v_F^2 p^2\right] \\ \alpha' &\equiv \alpha - v_F p\tilde{\zeta} = -\frac{\gamma_1 \alpha}{v_F^2 p^2 - \gamma_1} \\ C &\equiv -v_F p \left(\frac{v_F p}{\gamma_1}\right)^{N-1} - \frac{\gamma_4}{\gamma_0} v_F p \left(\frac{v_F p}{\gamma_1}\right)^{N-2} \zeta + (\epsilon + \mu)\left(\frac{v_F p}{\gamma_1}\right)^{N-1} \zeta \\ \delta &\equiv -\alpha \left(\frac{v_F p}{\gamma_1}\right)^{N-1} \zeta - \frac{\gamma_4}{\gamma_0} v_F p \left(\frac{v_F p}{\gamma_1}\right)^{N-2} \tilde{\zeta} + (\epsilon + \mu)\left(\frac{v_F p}{\gamma_1}\right)^{N-1} \tilde{\zeta} \\ \lambda &\equiv \alpha \left(\frac{v_F p}{\gamma_1}\right)^{N-1} \tilde{\zeta} = \xi_p \frac{\alpha^2}{v_F^2 p^2 - \gamma_1} \end{aligned}$$

Similarly we get for Eq. (71)

$$(B + \alpha')A_- = (C + \delta + \lambda)A_+. \tag{75}$$

In the low-energy limit that we consider below, $\xi_p, \epsilon, \alpha \ll \gamma_1$. In this limit

$$C \approx \xi_p \quad \text{and} \quad \delta \approx 0.$$

Combining Eqs. (74) and (75) gives

$$(B \pm \alpha')A_\mp = (C + \lambda)A_\pm. \tag{76}$$

The right hand side is with above approximations

$$(C + \lambda)A_\pm = \xi_p \left(1 + \frac{\alpha^2}{v_F^2 p^2 - \gamma_1^2}\right) A_\pm \tag{77}$$

and the left hand side is

$$\begin{aligned}(B \pm \alpha')A_\mp = \Big[&- \gamma_1 \left(\frac{v_F p}{\gamma_1}\right)^2 \frac{\gamma_1(\epsilon + \mu \pm \alpha) - (\gamma_4/\gamma_0)(v_F^2 p^2 + \gamma_1^2)}{v_F^2 p^2 - \gamma_1^2} \\ &- v_F p \frac{\gamma_4}{\gamma_0} \frac{v_F p}{\gamma_1} + (\epsilon + \mu \pm \alpha)\Big] A_\mp \end{aligned} \tag{78}$$

Together above equations give with help of Mathematica a pair of equations that couple the coefficients A_+ and A_-:

$$\xi_p A_\pm = \frac{\gamma_1}{\gamma_1^2 - v_F^2 p^2 - \alpha^2} \left[\gamma_1(\epsilon + \mu \pm \alpha) - 2\frac{\gamma_4}{\gamma_0} v_F^2 p^2\right] A_\mp \tag{79}$$

From here it is a straightforward calculation to solve the energy ϵ. When we set $(\alpha/\gamma_1)^2 \approx 0$ we get after some algebra that the dispersion relation of the surface states is

$$\epsilon = \mu_p \pm \sqrt{\xi_p^2 (1 - v_F^2 p^2/\gamma_1^2 - \alpha^2/\gamma_1^2)^2 + \alpha^2}, \tag{80}$$

where

$$\mu_p = \frac{p^2}{2m^*} - \mu, \quad m^* = \frac{\gamma_1 \gamma_0}{4\gamma_4 v_F^2}. \tag{81}$$

In the limit $N \to \infty$ the term $\xi_p \to 0$ and the dispersion becomes quadratic, $\epsilon = \mu_p \pm \alpha$. However, when $v_F p < \gamma_1$, it is suppressed by the effective mass $m^* \gg p/v_F$. Thus the energy band of the surface states is almost flat near the Dirac points. This is in a good agreement with the numerical diagonalization of the exact Hamiltonian, as seen in figure 10.

If we neglect the hopping γ_4, the term $\mu_p = 0$ and the band becomes totally flat in the bulk limit $N \to \infty$. This coincides with the above discussion about the topological properties of the bulk states. Since the hopping γ_4 appears in the bulk Hamiltonian (60) with the identity matrix, it breaks the symmetry condition $\{\sigma_z, H\}$ destroying the topological protection of the nodal line and thus the surface zero modes.

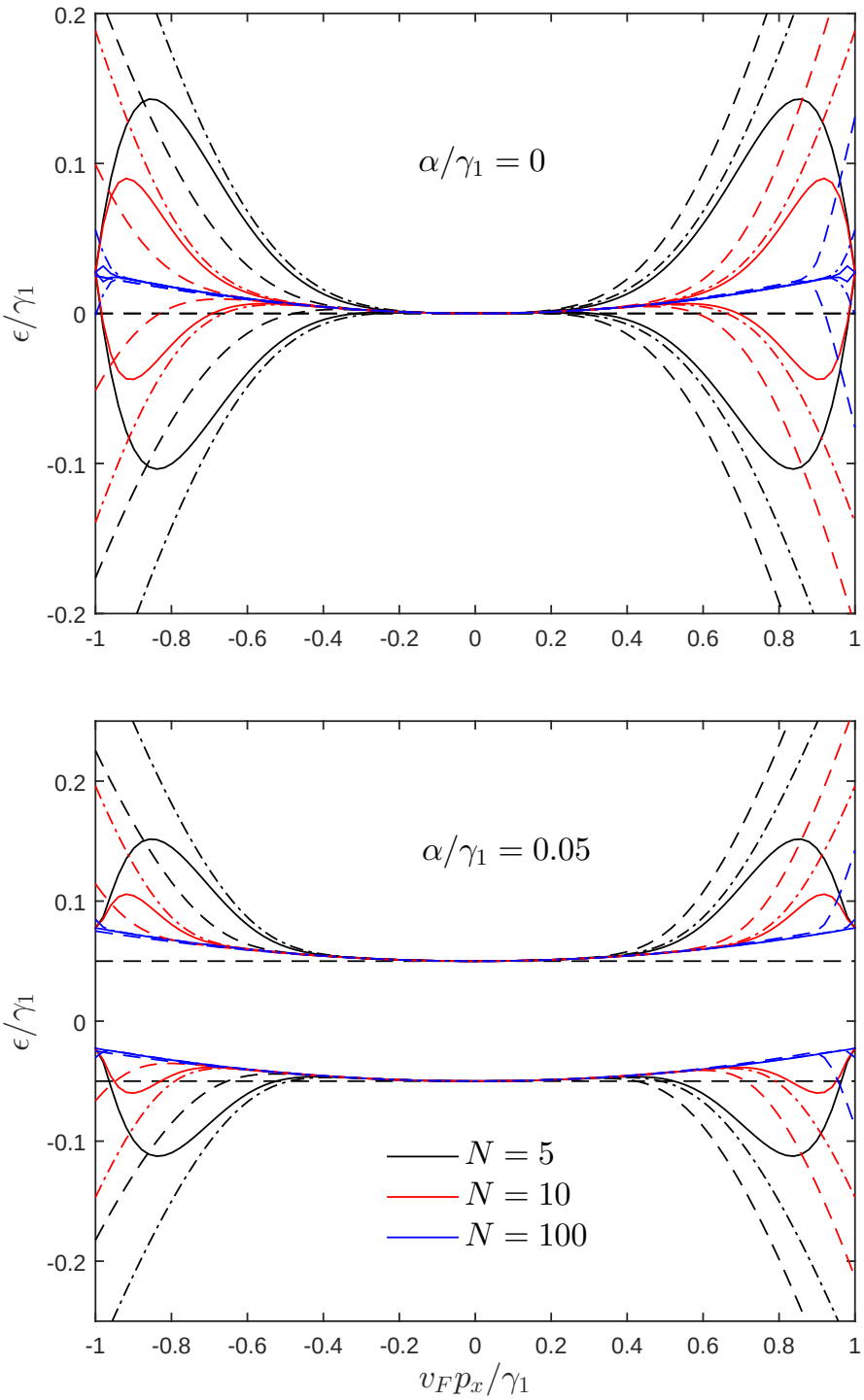

Figure 10: The analytical solutions Eq. (80) for $\alpha = 0$ and for $\alpha = 0.1\gamma_1$ with the numerical solutions. Solid lines are the analytical solutions, dashed lines are the numerically calculated energy states in x-direction and the dash-dotted ones correspond to y-direction. Above N is the number of layers. The staggering potential α splits the energy states and opens up a gap of 2α. The difference between the analytical and numerical solutions is mainly due to γ_3-term that is neglected in the analytical part.

5 Superconductivity

The phenomenon of superconductivity was discovered in 1911 when H. Kamerlingh Onnes studied the behaviour of materials at extreme low temperatures. Theorists of that time were desperate to explain the origin of this peculiar state of matter characterized by infinite electrical conductivity. Solving the nature of superconductivity became one of the hardest problems in physics in the 20th century. Many great names in the field of quantum mechanichs, such as Albert Einstein, Niels Bohr and Richard Feynman, were unable to solve it. Only phenomenological descriptions were proposed until in 1957 physicists Bardeen, Cooper and Schrieffer (BCS) published their ground breaking microscopic theory of superconductivity that was able to explain all the essential properties of superconducting matter. An important prediction of the theory is the role of *critical temperature* T_c below which the transformation into a superconducting state occurs. BCS showed that T_c is typically very low, a few Kelvin. This and other predictions agreed well with the experiments [20].

Understanding the mechanism of superconductivity invoked discussion about the possibility of the elevation of the critical temperature. This question was for the first time posed by Little in 1964. Since then theoretical models enabling high critical temperature have been under investigation and in 1986 Bednorz and Müller experimentally realized a new class of high-temperature superconductors [6]. Their properties have been found to be quite similar to conventional superconductors described by BCS theory. It is still an open question if the high-temperature superconducting state fundamentally differs from the BCS state. In the article on which this work rests on [16] the description of high-temperature surface superconductivity on graphite is based on BCS theory. Therefore I derive below crucial parts of the BCS theory. For that we need to assume the formation of Cooper pairs in the presence of an attractive interaction and that the pairing can be described with mean-field theory. These assumptions lead to a good agreement with the experiments in the case of conventional superconductor. It is, however, under investigation if the mean-field approximation is valid for the flat band met for example in graphite. In any case, it is useful to take the mean-field theory as a starting point to which the prospective more sophisticated theories can be compared.

5.1 Cooper pairs

In 1955 David Pines showed that the electron-phonon coupling in the lattice may create an attractive force between the electrons. The phenomenological idea is that an electron polarizes the media as it moves in the lattice. It attracts a positively charged ion which further attracts another electron. Hence it seems

as there were an attractive interaction between the two electrons [17]. Pines' work served as a starting point for L. N. Cooper who showed in 1956 that even a weak attractive interaction between electrons in the Fermi sea may couple electrons into bound pairs. He even showed that the Fermi sea of electrons is unstable against the formation of at least one Cooper pair, i.e., if there is an attractive interaction in the system, Cooper pairs will form [23].

The aim is to form a Hamiltonian operating in a Fock space that enables this kind of coupling between the electrons. For a general coupling potential the system would be too complicated to solve exactly so a few simplifications are made. The pair of electrons has the lowest energy when the total momentum vanishes. Hence we may assume the two electrons to have opposite momenta $(\mathbf{k}, -\mathbf{k})$. Often the pair is also taken to be in a spin singlet state, i.e., the electrons have opposite spins. This is the only spin state that does not break the rotational symmetry of the system. Also, if there are a lot of impurities in the matter, the amplitude $|\mathbf{k}|$ becomes the conserving quantity instead of the vector $\mathbf{k}$. Therefore the antisymmetric wavefunctions in $\mathbf{k}$ are averaged to zero and only the symmetric ones remain. Since the total electron wavefunction is antisymmetric, the spin part must be a singleton. Experiments have shown that for conventional superconductors the Cooper pairs are indeed in the spin singlet state. There are, however, also some other types of superconductors for which this does not hold, but they are left out of discussion here.

5.2 BCS-theory

Next we construct a *pairing Hamiltonian* that describes the superconducting state. It consists of a usual single-particle Hamiltonian that gives the kinetic energy and of a two-particle interaction term obeying the assumptions made above:

$$H = \sum_{\mathbf{k},\sigma} c^\dagger_{\mathbf{k}\sigma} H_{0\mathbf{k}} c_{\mathbf{k}\sigma} + \sum_{\mathbf{k},\mathbf{l}} V_{\mathbf{k}\mathbf{l}} c^\dagger_{\mathbf{k}\uparrow} c^\dagger_{-\mathbf{k}\downarrow} c_{-\mathbf{l}\downarrow} c_{\mathbf{l}\uparrow}, \tag{82}$$

where $H_{0\mathbf{k}}$ is the Hamiltonian of the non-interacting electron gas and the operator $c^\dagger_{\mathbf{k}\uparrow} c^\dagger_{-\mathbf{k}\downarrow}$ creates one Cooper pair at momentum $\mathbf{k}$.

The next crucial assumption is that the formation of a Cooper pair can be described by a mean-field theory, i.e., we can write

$$c_{-\mathbf{k}\downarrow} c_{\mathbf{k}\uparrow} = F_{\mathbf{k}} + \delta_{\mathbf{k}}\,, \tag{83}$$

where $F_{\mathbf{k}} = \langle c_{-\mathbf{k}\downarrow} c_{\mathbf{k}\uparrow} \rangle_{av}$ is the mean field or the correlation function and $\delta_{\mathbf{k}} = c_{-\mathbf{k}\downarrow} c_{\mathbf{k}\uparrow} - F_{\mathbf{k}}$ describes fluctuations around it. The function $F_{\mathbf{k}}$ is also called the pair amplitude and it measures the amount of correlated pairs. It plays an important role in the BCS-theory: it can be seen as an order parameter that

describes a phase transition from a normal state to a superconducting one. If $F_{\mathbf{k}} = 0$ there are no Cooper pairs and the system is in a normal state. For $|F_{\mathbf{k}}| > 0$ the amount of correlated pairs is finite and the material becomes superconducting.

Substituting Eq. (83) into the Hamiltonian (82) and neglecting the terms proportional to $\delta_{\mathbf{k}}^2$ gives

$$H = \sum_{\mathbf{k},\sigma} c_{\mathbf{k}\sigma}^\dagger H_{0\mathbf{k}} c_{\mathbf{k}\sigma} + \sum_{\mathbf{k}} (\Delta_{\mathbf{k}} c_{\mathbf{k}\uparrow}^\dagger c_{-\mathbf{k}\downarrow}^\dagger + \Delta_{\mathbf{k}}^* c_{-\mathbf{k}\downarrow} c_{\mathbf{k}\uparrow} - \Delta_{\mathbf{k}} F_{\mathbf{k}}^\dagger), \tag{84}$$

where

$$\Delta_{\mathbf{k}} \equiv \sum_{\mathbf{l}} V_{\mathbf{k}\mathbf{l}} F_{\mathbf{l}}. \tag{85}$$

This $\Delta_{\mathbf{k}}$ is called the pair potential and it can be chosen to be the order parameter of the superconducting state instead of $F_{\mathbf{k}}$. It is a complex number that quantifies the strength of pair formation.

Originally BCS diagonalized the Hamiltonian (84) by a variational calculation. Later Bogoliubov found a more elegant solution with a linear transformation into new fermion operators

$$\gamma_{\mathbf{k}\uparrow}^\dagger = u_{\mathbf{k}} c_{\mathbf{k}\uparrow}^\dagger + v_{\mathbf{k}} c_{-\mathbf{k}\downarrow} \tag{86}$$

$$\gamma_{\mathbf{k}\downarrow}^\dagger = u_{-\mathbf{k}} c_{-\mathbf{k}\downarrow}^\dagger - v_{-\mathbf{k}} c_{\mathbf{k}\uparrow}, \tag{87}$$

where $|u_{\mathbf{k}}|^2 + |v_{\mathbf{k}}|^2 = 1$. The operators $\gamma_{\mathbf{k}\sigma}^\dagger$, $\gamma_{\mathbf{k}\sigma}$ are called *Bogoliubov* operators. They manifest themselves as creation and annihilation operators of excitations in the superconducting state. Demanding that the operators (86) and (87) diagonalize the Hamiltonian (84), i.e.,

$$H = -E_0 + \sum_{\mathbf{k},\sigma} E_{\mathbf{k}} \gamma_{\mathbf{k}\sigma}^\dagger \gamma_{\mathbf{k}\sigma}, \tag{88}$$

gives conditions for coefficients $u_{\mathbf{k}}$ and $v_{\mathbf{k}}$. A useful trick for the calculation is to notice that the equation (88) is equivalent to

$$[H, \gamma_{\mathbf{k}\sigma}^\dagger] = \gamma_{\mathbf{k}\sigma}^\dagger E_{\mathbf{k}}. \tag{89}$$

This result can be verified by a straightforward calculation. We may assume that the allowed $\mathbf{k}$-states are symmetric around zero, so for every state $\mathbf{k}$ there exists a state $-\mathbf{k}$. Then the summation can be done either over $\mathbf{k}$ or $-\mathbf{k}$ and the Hamiltonian (84) can be written as

$$H = \sum_{\mathbf{k}} c_{\mathbf{k}\uparrow}^\dagger H_{0\mathbf{k}} c_{\mathbf{k}\uparrow} + c_{-\mathbf{k}\downarrow}^\dagger H_{0-\mathbf{k}} c_{-\mathbf{k}\downarrow} + \Delta_{\mathbf{k}} c_{\mathbf{k}\uparrow}^\dagger c_{-\mathbf{k}\downarrow}^\dagger + \Delta_{\mathbf{k}}^* c_{-\mathbf{k}\downarrow} c_{\mathbf{k}\uparrow} - \Delta_{\mathbf{k}} F_{\mathbf{k}}^\dagger. \tag{90}$$

Let us examine the commutator

$$[H, \gamma^\dagger_{\mathbf{k}\uparrow}] = [H, u_{\mathbf{k}} c^\dagger_{\mathbf{k}\uparrow}] + [H, v_{\mathbf{k}} c_{-\mathbf{k}\downarrow}]. \tag{91}$$

We see immediately that for most of the terms in the Hamiltonian the commutators with $u_{\mathbf{k}} c^\dagger_{\mathbf{k}\uparrow}$ and $v_{\mathbf{k}} c_{-\mathbf{k}\downarrow}$ vanish, since for any fermion operator $c_\nu c_\nu = c^\dagger_\nu c^\dagger_\nu \equiv 0$. Using the fermion anticommutator rules the remaining terms are

$$\begin{aligned}
&[c^\dagger_{\mathbf{k}\uparrow} H_{0\mathbf{k}} c_{\mathbf{k}\uparrow}, u_{\mathbf{k}} c^\dagger_{\mathbf{k}\uparrow}] = c^\dagger_{\mathbf{k}\uparrow} H_{0\mathbf{k}} u_{\mathbf{k}} \\
&[\Delta^*_{\mathbf{k}} c_{-\mathbf{k}\downarrow} c_{\mathbf{k}\uparrow}, u_{\mathbf{k}} c^\dagger_{\mathbf{k}\uparrow}] = c_{-\mathbf{k}\downarrow} \Delta^*_{\mathbf{k}} u_{\mathbf{k}} \\
&[c^\dagger_{-\mathbf{k}\downarrow} H_{0-\mathbf{k}} c_{-\mathbf{k}\downarrow}, v_{\mathbf{k}} c_{-\mathbf{k}\downarrow}] = -c_{-\mathbf{k}\downarrow} H_{0-\mathbf{k}} v_{\mathbf{k}} \\
&[\Delta_{\mathbf{k}} c^\dagger_{\mathbf{k}\uparrow} c^\dagger_{-\mathbf{k}\downarrow}, v_{\mathbf{k}} c_{-\mathbf{k}\downarrow}] = c^\dagger_{\mathbf{k}\uparrow} \Delta_{\mathbf{k}} v_{\mathbf{k}}.
\end{aligned}$$

Equating the sum of these commutators to $\gamma^\dagger_{\mathbf{k}\uparrow} E_{\mathbf{k}} = c^\dagger_{\mathbf{k}\uparrow} E_{\mathbf{k}} u_{\mathbf{k}} + c_{-\mathbf{k}\downarrow} E_{\mathbf{k}} v_{\mathbf{k}}$ gives us a matrix equation

$$\begin{pmatrix} H_{0\mathbf{k}} & \Delta_{\mathbf{k}} \\ \Delta^*_{\mathbf{k}} & -H_{0-\mathbf{k}} \end{pmatrix} \begin{pmatrix} u_{\mathbf{k}} \\ v_{\mathbf{k}} \end{pmatrix} = E_{\mathbf{k}} \begin{pmatrix} u_{\mathbf{k}} \\ v_{\mathbf{k}} \end{pmatrix}. \tag{92}$$

Similarly from the condition $[H, \gamma^\dagger_{\mathbf{k}\downarrow}] = \gamma^\dagger_{\mathbf{k}\downarrow} E_{\mathbf{k}}$ we get

$$\begin{pmatrix} H_{0-\mathbf{k}} & \Delta_{\mathbf{k}} \\ \Delta^*_{\mathbf{k}} & -H_{0\mathbf{k}} \end{pmatrix} \begin{pmatrix} u_{-\mathbf{k}} \\ v_{-\mathbf{k}} \end{pmatrix} = E_{\mathbf{k}} \begin{pmatrix} u_{-\mathbf{k}} \\ v_{-\mathbf{k}} \end{pmatrix}. \tag{93}$$

If we assume that the potential $V_{\mathbf{kl}}$ is inversion symmetric, i.e., $V_{\mathbf{kl}} = V_{-\mathbf{k}-\mathbf{l}}$ and also the correlation function $F_{\mathbf{k}} = F_{-\mathbf{k}}$ we get $\Delta_{\mathbf{k}} = \Delta_{-\mathbf{k}}$. Then by changing the indices $\mathbf{k} \to -\mathbf{k}$ Eq. (93) gives exactly Eq. (92), since $E_{\mathbf{k}} = E_{-\mathbf{k}}$. Equation (92) is called the Bogoliubov-de Gennes (BdG) equation and it can be understood as the Schrödinger equation for the superconducting state. Indeed, if the order parameter $\Delta_{\mathbf{k}} = 0$, the Eq. (92) decouples into

$$\begin{aligned}
H_{0\mathbf{k}} u_{\mathbf{k}} &= E_{\mathbf{k}} u_{\mathbf{k}} \quad \text{and} \\
H_{0-\mathbf{k}} v_{\mathbf{k}} &= -E_{\mathbf{k}} v_{\mathbf{k}},
\end{aligned}$$

which are the Schrödinger equations for electrons and holes.

The eigenenergies $E_{\mathbf{k}}$ of the superconducting state and the coefficients $u_{\mathbf{k}}$ and $v_{\mathbf{k}}$ can be determined from the BdG equation. The eigenenergies are

$$E_{\mathbf{k}} = \pm\sqrt{\xi^2_{\mathbf{k}} + |\Delta_{\mathbf{k}}|^2}, \tag{94}$$

where $\xi_{\mathbf{k}} = \hbar^2 \mathbf{k}^2/(2m) - \mu$, the single electron energy. From here we see that the function $\Delta_{\mathbf{k}}$ opens up a gap into the energy spectrum, which is why it is also

called the gap function. The corresponding eigenstates for positive energies $E_{\mathbf{k}} > 0$ are

$$u_{\mathbf{k}} = \frac{1}{\sqrt{2}}\sqrt{1 + \frac{\xi_{\mathbf{k}}}{E_{\mathbf{k}}}}e^{i\phi}$$
$$v_{\mathbf{k}} = \frac{1}{\sqrt{2}}\sqrt{1 - \frac{\xi_{\mathbf{k}}}{E_{\mathbf{k}}}}. \tag{95}$$

Here the phase factor is the phase of $\Delta_{\mathbf{k}} = |\Delta_{\mathbf{k}}|e^{i\phi}$.

5.3 Self-consistency equation

The gap function $\Delta_{\mathbf{k}}$ can be calculated self-consistently from the BdG equation. If we assume the inversion symmetry for the dispersion, i.e., $u_{\mathbf{k}} = u_{-\mathbf{k}}$ and $v_{\mathbf{k}} = v_{-\mathbf{k}}$, the inverse transformation of (87) and (86) is

$$c_{\mathbf{k}\uparrow} = u_{\mathbf{k}}\gamma_{\mathbf{k}\uparrow} - v^*_{\mathbf{k}}\gamma^\dagger_{\mathbf{k}\uparrow}$$
$$c_{-\mathbf{k}\downarrow} = u_{\mathbf{k}}\gamma_{\mathbf{k}\downarrow} + v^*_{\mathbf{k}}\gamma^\dagger_{\mathbf{k}\uparrow}.$$

If the above transformations are substituted into definition (85) we get

$$\begin{aligned}\Delta_{\mathbf{k}} &\equiv \sum_{\mathbf{l}} V_{\mathbf{k}\mathbf{l}}u_{\mathbf{l}}v^*_{\mathbf{l}}\left\langle 1 - \gamma^*_{\mathbf{l}\downarrow}\gamma_{\mathbf{l}\downarrow} - \gamma^*_{\mathbf{l}\uparrow}\gamma_{\mathbf{l}\uparrow}\right\rangle \\ &= \sum_{\mathbf{l}} V_{\mathbf{k}\mathbf{l}}u_{\mathbf{l}}v^*_{\mathbf{l}}\left\langle 1 - n_{\mathbf{l}\downarrow} - n_{\mathbf{l}\uparrow}\right\rangle,\end{aligned} \tag{96}$$

where $n_{\mathbf{l}\sigma}$ is the number operator of excitations. Since the excitations obey Fermi statistics, the average number of excitations in an energy state $E_{\mathbf{l}}$ is given by the Fermi function

$$f(E_{\mathbf{l}}) = \frac{1}{e^{\beta E_{\mathbf{l}}} + 1} \tag{97}$$

with $\beta = 1/k_B T$. Hence we may write

$$\Delta_{\mathbf{k}} = \sum_{\mathbf{l}} V_{\mathbf{k}\mathbf{l}}u_{\mathbf{l}}v^*_{\mathbf{l}}[1 - 2f(E_{\mathbf{l}})] \tag{98}$$

if we assume that the energy does not depend on spin. This is a useful form for the self-consistency equation in general since it depends only on the eigenenergies $E_{\mathbf{k}}$ and the coefficients $u_{\mathbf{k}}$ and $v_{\mathbf{k}}$, which can be solved from the BdG-equation (92) numerically if needed. Substitution of these values into the definition (98) gives a new value for $\Delta_{\mathbf{k}}$, which can be further substituted into

BdG equation to solve new values for $E_{\mathbf{k}}, u_{\mathbf{k}}$ and $v_{\mathbf{k}}$. In this way a numerical approximation for $\Delta_{\mathbf{k}}$ is obtained. In the BCS ground state, however, the self-consistency equation can be solved analytically using the solutions (94) and (95)written above. We do this next.

First we must recall that the Bogoliubov operators operate on the BCS-ground state like the creation and annihilation operators on the Fermi sea. Then the expectation value of the number operator is

$$\langle BCS|\, n_{\mathbf{l}\sigma}\, |BCS\rangle = \begin{cases} 1 & \text{for } E_{\mathbf{l}} < 0 \\ 0 & \text{for } E_{\mathbf{l}} > 0, \end{cases} \tag{99}$$

where we set the Fermi energy $E_F = 0$. Replacing the sum in Eq. (96) by an integral and substituting the expectation values gives

$$\Delta_{\mathbf{k}} = -\int\limits_{E_{\mathbf{l}}<0} \frac{\mathrm{d}^{(3)}\mathbf{l}}{(2\pi)^3} V_{\mathbf{kl}} u_{\mathbf{l}} v_{\mathbf{l}}^* + \int\limits_{E_{\mathbf{l}}>0} \frac{\mathrm{d}^{(3)}\mathbf{l}}{(2\pi)^3} V_{\mathbf{kl}} u_{\mathbf{l}} v_{\mathbf{l}}^*. \tag{100}$$

To proceed we need to find an approximate form for the potential $V_{\mathbf{kl}}$. Originally Cooper introduced a simple model in which the potential is constant $V_{\mathbf{kl}} = -W$ below some cutoff energy E_c and zero above it. This approximation is serviceable, since the attractive interaction originates from phonon interaction and the phonon spectrum has cutoff energy characterized by Debye energy $\hbar\omega_D$ [23]. Hence the potential

$$V_{\mathbf{kl}} = \begin{cases} -W & \text{for } |E_{\mathbf{l}}| < E_c \\ 0 & \text{otherwise} \end{cases} \tag{101}$$

is independent of $\mathbf{k}$ and also $\Delta_{\mathbf{k}} = \Delta$.

From Eq. (95) for $u_{\mathbf{k}}$ and $v_{\mathbf{k}}$ we get via a direct calculation

$$u_{\mathbf{l}} v_{\mathbf{l}}^* = \frac{1}{2}\frac{\Delta}{E_{\mathbf{l}}}. \tag{102}$$

Now the integrands depend only on $E_{\mathbf{l}}$ and we can combine the two integrals. So

$$\Delta = -\frac{W}{2}\int\limits_0^{E_c} \frac{\mathrm{d}^{(3)}\mathbf{l}}{(2\pi)^3}\frac{\Delta}{E_{\mathbf{l}}}. \tag{103}$$

In order to calculate the integral we need to do a change of variables. The number of states in a volume of parameter space is

$$\frac{\mathrm{d}^{(3)}\mathbf{l}}{(2\pi)^3} = \nu(\xi_{\mathbf{l}})\mathrm{d}\xi_{\mathbf{l}} = \eta(E_{\mathbf{l}})\mathrm{d}E_{\mathbf{l}}, \tag{104}$$

where ν and η are the densities of states in $\xi_{\mathbf{l}}$- and $E_{\mathbf{l}}$-spaces. Since the main contribution comes from the states near the Fermi surface $\xi_{\mathbf{l}} = 0$, we may approximate $\nu(\xi_{\mathbf{l}}) \approx \nu(0)$. Then we get

$$\eta(E_{\mathbf{l}}) \approx \nu(0)\frac{\mathrm{d}\xi_{\mathbf{l}}}{\mathrm{d}E_{\mathbf{l}}} = \nu(0)\frac{E_{\mathbf{l}}}{\sqrt{E_{\mathbf{l}}^2 - |\Delta|^2}} \tag{105}$$

for $|E_{\mathbf{l}}| \geq |\Delta|$. Since there are no states inside the energy gap $2|\Delta|$, we have $\eta(|E_{\mathbf{l}}| < |\Delta|) = 0$. Finally we get the BCS self-consistency equation

$$\Delta = -W\nu(0)\int_{\Delta}^{E_c} \frac{\mathrm{d}E_{\mathbf{l}}\Delta}{\sqrt{E_{\mathbf{l}}^2 - |\Delta|^2}}. \tag{106}$$

We find immediately a trivial solution $\Delta = 0$ which corresponds to the normal state. When searching the non-trivial solution we may assume Δ to be finite and divide it from both sides of Eq. (106). Integrating the remaining right hand side gives us

$$1 = -W\nu(0)\ln\left(\frac{E_c + \sqrt{E_c^2 - |\Delta|^2}}{|\Delta|}\right).$$

Since the cutoff energy E_c is of the order of Debye energy, we have $E_c \gg |\Delta|$ and then

$$1 \approx -W\nu(0)\ln\left(\frac{2E_c}{|\Delta|}\right) \quad \text{or} \quad |\Delta| \approx 2E_c \exp\left(-\frac{1}{W\nu(0)}\right). \tag{107}$$

Hence the order parameter Δ depends exponentially on the interaction strength W, which is the reason why superconductivity generally appears at very low temperatures.

6 Superconducting state of Graphite

6.1 BdG equation

In this section the BdG equations are derived and solved for graphite using the tight-binding model described in section 4. The aim is to define the surface states of graphite when superconductivity is added to the model. The calculations follow the reference [16] but with the addition of the on-site potential α. Above the Hamiltonian for holes is separate from and symmetric to the electron Hamiltonian. In the superconducting state the electrons and holes are coupled through the order-parameter field Δ as stated above. The Hamiltonian for holes can be expressed in terms of the electron Hamiltonian (55) as $H^{(h)}(\mathbf{K},\mathbf{p}) = H^*(\mathbf{K}',-\mathbf{p}) = H^*(-\mathbf{K},-\mathbf{p})$. Linearizing the tight-binding Hamiltonian (41) around the Dirac point $-\mathbf{K}$ similarly as done in the section 4.1 gives relations

$$\begin{aligned}
\hat{H}^{(0)}_{nm}(-\mathbf{K},\mathbf{p}) =& v_F(-(\hat{\boldsymbol{\sigma}}\cdot\mathbf{p})^* + \alpha\hat{\sigma}_z)\delta_{mn} \\
\hat{H}^{(1)}_{nm}(-\mathbf{K},\mathbf{p}) =& \hat{H}^{(1)*}_{nm}(\mathbf{K},\mathbf{p}) \\
\hat{H}^{(l)}_{nm}(-\mathbf{K},\mathbf{p}) =& -\hat{H}^{(l)*}_{nm}(\mathbf{K},\mathbf{p}) \quad \text{for} \quad l = 3,4.
\end{aligned}$$

Since $\hat{H}^{(1)}_{nm}$ is independent of $\mathbf{p}$ and other terms are linear in it, we get for the hole Hamiltonian $\hat{H}^{(hl)}(\mathbf{K},\mathbf{p}) = \hat{H}^{(l)}(\mathbf{K},\mathbf{p})$ for all l. Then

$$\begin{aligned}
H^h_{\mathbf{K}} =& \sum_{l,\mathbf{p}}\sum_{n,m=1}^{N} \hat{\psi}^{(h)\dagger}_n(\mathbf{p})\hat{H}^{(hl)}(\mathbf{K},\mathbf{p})\hat{\psi}^{(h)}_m \\
=& \sum_{l,\mathbf{p}}\sum_{n,m=1}^{N} \hat{\psi}^{(h)\dagger}_n(\mathbf{p})\hat{H}^{(l)}(\mathbf{K},\mathbf{p})\hat{\psi}^{(h)}_m \\
=& \sum_{\mathbf{p}}\sum_{n,m=1}^{N} \hat{\psi}^{(h)\dagger}_n(\mathbf{p})\hat{H}_{nm}(\mathbf{K},\mathbf{p})\hat{\psi}^{(h)}_m.
\end{aligned}$$

Below the electron wave function is denoted by $\hat{u}_n = \hat{\psi}_n$ and the hole wave function is $\hat{v}_n = \hat{\psi}^{(h)}_n$. While the electron interaction energy ϵ is measured upwards from the chemical potential μ, i.e., $E = \mu + \epsilon$, the energy of holes is measured from the chemical potential downwards, $E = \mu - \epsilon$. As the Hamiltonian for normal graphite is a $2N \times 2N$-matrix, where N is the number of layers, the superconducting Hamiltonian is a $4N \times 4N$-matrix

$$\sum_m \check{\tau}_3 \otimes \left[\hat{H}_{nm}(\mathbf{K},\mathbf{p}) - \mu\delta_{nm}\right]\check{\Psi}_m + \check{\Delta}_n\check{\Psi}_n = \epsilon\check{\Psi}_n, \tag{108}$$

analogously to Eq. (92). Here

$$\check{\tau}_3 = \begin{pmatrix} 1 & 0 \\ 0 & -1 \end{pmatrix}, \check{\Delta}_n = \begin{pmatrix} 0 & \Delta_n \\ \Delta_n^* & 0 \end{pmatrix}, \check{\Psi}_n = \begin{pmatrix} \hat{u}_n \\ \hat{v}_n \end{pmatrix}$$

are objects in the Nambu space. The components of the Nambu vector $\check{\Psi}_n$ are pseudospinors

$$\hat{u}_n = \begin{pmatrix} u_n^1 \\ u_n^2 \end{pmatrix}, \quad \hat{v}_n = \begin{pmatrix} v_n^1 \\ v_n^2 \end{pmatrix}, \tag{109}$$

where the indices 1,2 refer to different sublattices. In section 4 we note that the parameter γ_3 does not affect the existence of the flat band. Hence we may set $\gamma_3 = 0$ in the BdG equation (108). For $n \neq 1,N$ Eq. (108) can be written in components as

$$\begin{aligned} \Big[v_F(\hat{\boldsymbol{\sigma}} \cdot \mathbf{p} + \sigma_z \alpha)\hat{u}_n - \gamma_1 \left(e^{i\pi/6}\sigma_- \hat{u}_{n+1} + e^{-i\pi/6}\sigma_+ \hat{u}_{n-1} \right) \\ + \frac{\gamma_4}{\gamma_0} \left(e^{i\pi/6} v_F p_- \hat{u}_{n+1} + e^{-i\pi/6} v_F p_+ \hat{u}_{n-1} \right) - \mu \hat{u}_n \Big] \\ + \Delta_n \hat{v}_n = \epsilon \hat{u}_n, \end{aligned} \tag{110}$$

$$\begin{aligned} -\Big[v_F(\hat{\boldsymbol{\sigma}} \cdot \mathbf{p} + \sigma_z \alpha)\hat{v}_n - \gamma_1 \left(e^{i\pi/6}\sigma_- \hat{v}_{n+1} + e^{-i\pi/6}\sigma_+ \hat{v}_{n-1} \right) \\ + \frac{\gamma_4}{\gamma_0} \left(e^{i\pi/6} v_F p_- \hat{v}_{n+1} + e^{-i\pi/6} v_F p_+ \hat{v}_{n-1} \right) - \mu \hat{v}_n \Big] \\ + \Delta_n^* \hat{u}_n = \epsilon \hat{v}_n \end{aligned} \tag{111}$$

For upcoming calculations it is useful to write the above equations in a different basis. Instead of electron and hole wave functions with sublattice components we define new spinors localized at each sublattice

$$\hat{\psi}^+ = \begin{pmatrix} 1 \\ 0 \end{pmatrix}, \quad \hat{\psi}^- = \begin{pmatrix} 0 \\ 1 \end{pmatrix}.$$

With these spinors the wave function is decomposed as

$$\check{\Psi}_n = \left[\begin{pmatrix} \alpha_n^+ \\ \beta_n^+ \end{pmatrix} \otimes \hat{\psi}^+ + \begin{pmatrix} \alpha_n^- \\ \beta_n^- \end{pmatrix} \otimes \hat{\psi}^- \right], \tag{112}$$

where

$$\check{\alpha}_n^\pm = \begin{pmatrix} \alpha_n^\pm \\ \beta_n^\pm \end{pmatrix} \tag{113}$$

is a vector in the Nambu space. With these notations

$$\hat{u}_{n=} \begin{pmatrix} \alpha_n^+ \\ \alpha_n^- \end{pmatrix} \quad \text{and} \quad \hat{v}_{n=} \begin{pmatrix} \beta_n^+ \\ \beta_n^- \end{pmatrix}. \tag{114}$$

Substitution of these vectors into Eq. (110) and setting $n = 1$ or $n = N$ gives two-component equations for the surface states. The components not containing γ_1 read

$$v_F p e^{-i\phi} \check{\tau}_3 \check{\alpha}_1^- + \alpha \check{\tau}_3 \check{\alpha}_1^+ + \frac{\gamma_4}{\gamma_0} v_F p e^{-i\phi + i\pi/6} \check{\tau}_3 \check{\alpha}_2^+ - \mu \check{\tau}_3 \check{\alpha}_1^+ + \check{\Delta}_1 \check{\alpha}_1^+ = \epsilon \check{\alpha}_1^+, \quad (115)$$

$$v_F p e^{i\phi} \check{\tau}_3 \check{\alpha}_N^+ - \alpha \check{\tau}_3 \check{\alpha}_N^- + \frac{\gamma_4}{\gamma_0} v_F p e^{i\phi - i\pi/6} \check{\tau}_3 \check{\alpha}_{N-1}^- - \mu \check{\tau}_3 \check{\alpha}_N^- + \check{\Delta}_N \check{\alpha}_N^- = \epsilon \check{\alpha}_N^-, \quad (116)$$

which uses the fact that $\hat{u}_n, \hat{v}_n = 0$ for $n = 0$ and $n = N + 1$.

6.2 Superconducting surface states

Next we assume that superconductivity emerges only in the surface states, i.e., $\Delta_n = 0$ for $n \neq 1,N$, The approximation is valid for $\Delta \ll \gamma_1$ and is suggested by the numerical consideration of the full BdG equations [16]. Now the equations (110) and (111) reduce to the Schrödinger equation of graphite bulk states and we may make an Ansatz analogous to the Ansatz (67) for the normal state:

$$\check{\alpha}_n^+ = \frac{C}{\sqrt{2}} e^{i(\psi - \pi/6)(n-1-\frac{N}{2})} \left[\left(\frac{v_F p}{\gamma_1} \right)^{n-1} \check{A}^+ + \left(\frac{v_F p}{\gamma_1} \right)^{N-n} \check{\zeta}_1 \check{A}^- \right], \quad (117)$$

$$\check{\alpha}_n^- = \frac{C}{\sqrt{2}} e^{i(\psi - \pi/6)(n-1-\frac{N}{2})} \left[\left(\frac{v_F p}{\gamma_1} \right)^{n-1} \check{\zeta}_2 \check{A}^+ + \left(\frac{v_F p}{\gamma_1} \right)^{N-n} \check{A}^- \right] e^{i\phi}. \quad (118)$$

Here $\check{A}^\pm = (A^\pm, B^\pm)^T$ are arbitrary constants not depending on n and C is a normalization constant. The matrices $\check{\zeta}_{\frac{1}{2}}$ are defined

$$\check{\zeta}_{\frac{1}{2}} = \left(\frac{v_F p}{\gamma_1} \right) \frac{\gamma_1 (\check{\tau}_3 \epsilon + \mu \pm \alpha) - (\gamma_4/\gamma_0)(v_F^2 p^2 - \gamma_1^2)}{v_F^2 p^2 - \gamma_1^2} = \begin{pmatrix} \zeta^e_{\frac{1}{2}} & 0 \\ 0 & \zeta^h_{\frac{1}{2}} \end{pmatrix} \quad (119)$$

The substitution of this Ansatz into equations (115) and (116) leads to a very similar calculation to that already carried through in Sec. 4.4. Since it is straightforward, I only introduce the result

$$\check{\tau}_3 \xi_p \check{A}^- = (\tilde{\epsilon} - \check{\tau}_3 (\tilde{\mu}_p + \tilde{\alpha})) \check{A}^+ - \check{\Delta}_1 \check{A}^+, \quad (120)$$

$$\check{\tau}_3 \xi_p \check{A}^+ = (\tilde{\epsilon} - \check{\tau}_3 (\tilde{\mu}_p - \tilde{\alpha})) \check{A}^- - \check{\Delta}_N \check{A}^-, \quad (121)$$

where

$$\tilde{\epsilon} = \epsilon (1 - v_F^2 p^2 / \gamma_1^2)^{-1}, \quad \tilde{\mu}_p = \mu_p (1 - v_F^2 p^2 / \gamma_1^2)^{-1} \quad \text{and}$$
$$\tilde{\alpha} = \alpha (1 - v_F^2 p^2 / \gamma_1^2)^{-1}.$$

The factor μ_p is defined as in (81) and ξ_p as in (73). This system of equations reduces after some algebra to a condition for the energy $\tilde{\epsilon}$

$$\begin{aligned}&(\tilde{\epsilon}^2-(\tilde{\mu}_p+\tilde{\alpha})^2-|\Delta_1|^2)(\tilde{\epsilon}^2-(\tilde{\mu}_p-\tilde{\alpha})^2-|\Delta_N|^2)\\&+\xi_p^4-\xi_p^2[2\tilde{\epsilon}^2+2\tilde{\mu}_p^2-2\tilde{\alpha}^2-\Delta_1^*\Delta_N-\Delta_1\Delta_N^*]=0.\end{aligned}\tag{122}$$

From here we can solve the allowed energy states at the surface. They are

$$\begin{aligned}\tilde{\epsilon}^2=&\frac{1}{2}(|\Delta_1|^2+|\Delta_N|^2)+\tilde{\mu}_p^2+\tilde{\alpha}^2+\xi_p^2\\&\pm\frac{1}{2}\Big[16\tilde{\mu}_p^2(\tilde{\alpha}^2+\xi_p^2)+(|\Delta_1|^2-|\Delta_N|^2)^2\\&+8\tilde{\alpha}\tilde{\mu}_p(|\Delta_1|^2-|\Delta_N|^2)+4\xi^2|\Delta_1-\Delta_N|^2\Big]^{\frac{1}{2}}.\end{aligned}\tag{123}$$

If also $\Delta_1=\Delta_N\equiv\Delta$ we get a somewhat simpler solution

$$\tilde{\epsilon}^2=(\tilde{\mu}_p\pm\sqrt{\tilde{\alpha}^2+\xi_p^2})^2+|\Delta|^2.\tag{124}$$

Writing the above equation in the form

$$\epsilon^2=\left(\mu_p\pm\sqrt{\xi_p^2(1-v_F^2p^2/\gamma_1^2)^2+\alpha^2}\right)^2+|\Delta|^2(1-v_F^2p^2/\gamma_1^2)^2\tag{125}$$

shows that these are the energy states of the normal state (80) with a gap $2|\Delta|(1-v_F^2p^2/\gamma_1^2)$ and without the correction $-\alpha^2/\gamma_1^2$ in the coefficient of ξ_p^2. This differs from a BCS superconductor whose eigenenergies (94) are the normal state energies with a gap $2|\Delta|$. If we set $\alpha=0$, the dispersion in the article [16] is obtained:

$$\tilde{\epsilon}^2=(\tilde{\mu}_p\pm\xi_p)^2+|\Delta|^2,\tag{126}$$

From Eqs. (124) and (126) one sees that there are four independent energy states on the surface. They correspond to electrons and holes in each valley.

We solved the exact BdG-matrix also numerically. The self-consistency equation used for the gap function Δ_n in the numerics is

$$\Delta_n=\int\frac{\mathrm{d}^2p}{(2\pi\hbar)^2}\sum_q W\mathrm{Tr}[\hat{u}_n(\mathbf{p},k)\hat{v}_n^*(\mathbf{p},k)]\cdot[1-2f(E_{\mathbf{p},k})],\tag{127}$$

where we assumed the 3D coupling potential is constant for each layer $V_{\mathbf{kl}}=W$. This is analogous to Eq. (98) derived above. Here the trace averages the eigenvectors over the two valleys. The sum goes over all the states corresponding to

a given 2D momentum $\mathbf{p}$ and the sum over $\mathbf{l}$ in Eq. (98) has been converted to an integral over p.

For the case $\alpha = 0$ the analytical approximation (126) works quite well as seen in Fig. 11. The deviations from the numerical solution, that is calculated from the full Hamiltonian (108) with $\gamma_3 = 0$, take place in the regime $v_F p/\gamma_1 > 0.5$. This is due to the assumption of small p made in the approximation. In all the plots $\gamma_3 = 0$, so $\epsilon(p_x) = \epsilon(p_y)$. The number of layers $N = 20$ gives already a good correspondence to the analytical flat band limit: increasing the number of layers to $N = 100$ does not essentially change the figure. Also for non-zero α and μ our model seems to correspond to the numerical solution. In Figs. 12 and 13 we see that the order parameters for different surfaces may differ if $\alpha \neq 0$. This breaks also the degeneracy in the energies of different surfaces. In Fig. 13 it seems that the chemical potential suppresses the effect of α and produces the same kind of dispersion to the other surface as in Fig. 11.

We see that by breaking the $A - B$-symmetry of the graphene sheet α destroys also the symmetry of graphite surface states. The top and bottom layers are no more equivalent and the order parameters for them differ. On the other hand, for $\alpha = 0.03$ the superconductivity is totally suppressed. Then the energy bands correspond to the non-superconducting dispersion in Fig. 10. Below we study closer the possible values of $\Delta_{1,N}$ as a function of α and discuss the limit of critical doping.

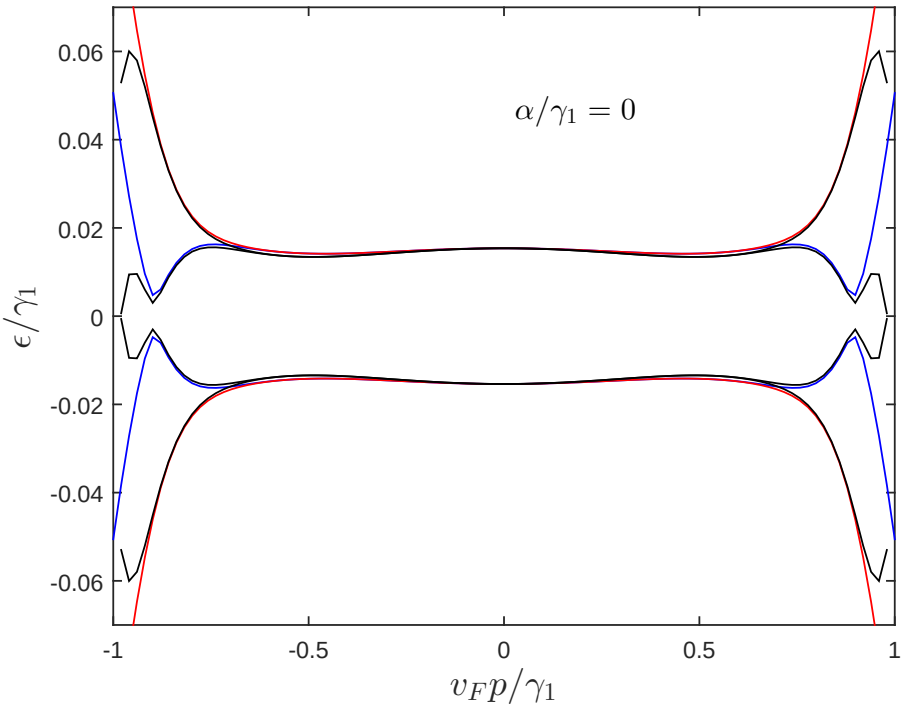

Figure 11: Lowest energy states for superconducting graphite with $\alpha = 0$. The gap Δ_n was calculated iteratively form Eq. (127) with a coupling constant $g = 0.5\,\gamma_1$ resulting to $\Delta_1 = \Delta_N = 0.015\,\gamma_1$. Red and blue lines are the numerically solved BdG eigenstates with the number of layers $N = 20$ and black lines are the analytical approximation Eq. (126).

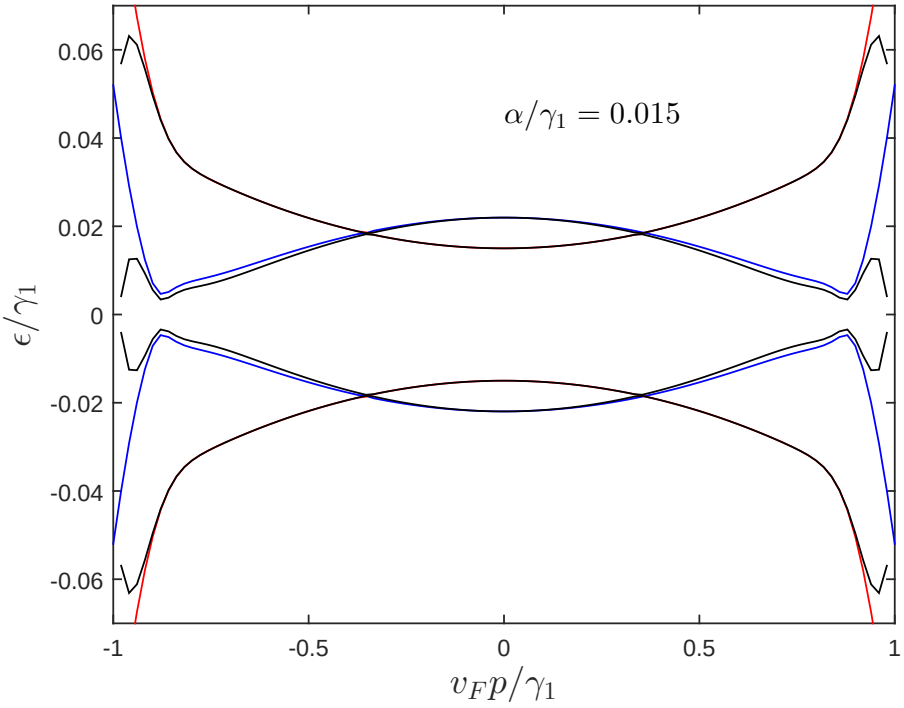

Figure 12: In this plot $N = 20$, $\alpha = 0.015\,\gamma_1$ and $g = 0.5\,\gamma_1$ yielding order parameters $\Delta_1 = 0.0001\,\gamma_1$ and$\Delta_N = 0.016\,\gamma_1$. Black lines are the analytical approximation Eq. (123) and blue and red lines are the numerical solution.

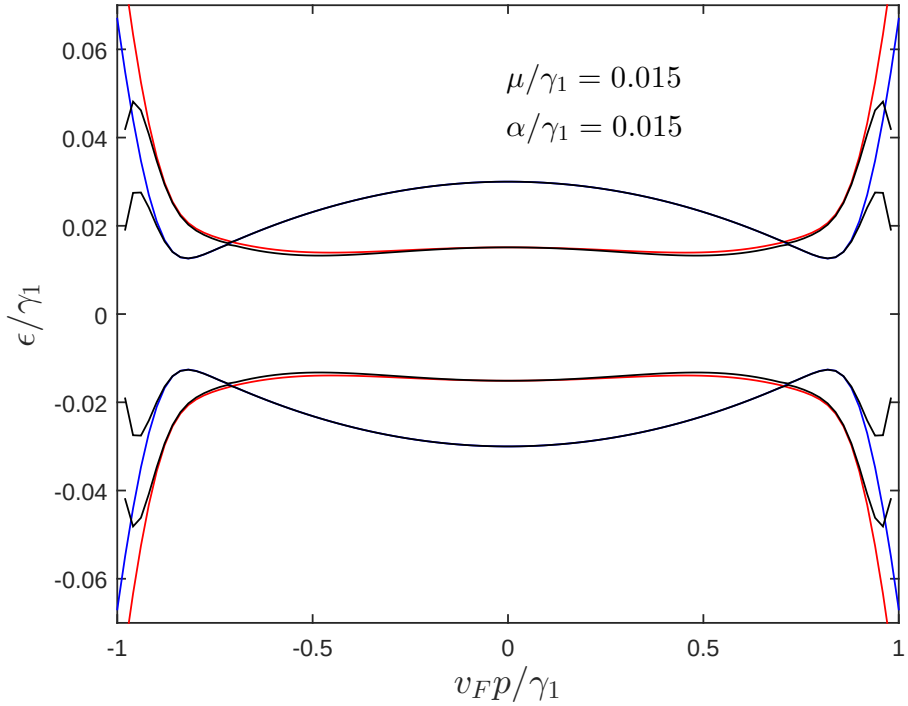

Figure 13: Here $N = 20$, $\alpha = 0.015\,\gamma_1$, $\mu = 0.015\,\gamma_1$ and $g = 0.5\,\gamma_1$ which gives the order parameters $\Delta_1 = 0.015\,\gamma_1$ and $\Delta_N = -0.0006\,\gamma_1$. The negative value for Δ_N is probably a result of numerical inaccuracy. Black lines are the analytical approximation Eq. (123) and blue and red lines are the numerical solution.

6.3 Self-consistency equation in the flat band limit

Next we solve the surface eigenstates in the flat band limit $N \to \infty$ and use them to calculate an analytical approximation for the self-consistency equation. Inside the flat band region $p < p_{FB} = \gamma_1/v_F$ we have $\xi_p = (p/p_{FB})^N = 0$. Now Eqs. (120) and (121) decouple giving

$$(\tilde{\epsilon}_1 - \check{\tau}_3(\tilde{\mu}_p + \tilde{\alpha}))\check{A}^+ = \check{\Delta}_1\check{A}^+ \tag{128}$$
$$(\tilde{\epsilon}_N - \check{\tau}_3(\tilde{\mu}_p - \tilde{\alpha}))\check{A}^- = \check{\Delta}_N\check{A}^-. \tag{129}$$

and the corresponding energies are obtained from Eq. (122):

$$(\tilde{\epsilon}^2 - (\tilde{\mu}_p + \tilde{\alpha})^2 - |\Delta_1|^2)(\tilde{\epsilon}^2 - (\tilde{\mu}_p - \tilde{\alpha})^2 - |\Delta_N|^2) = 0.$$

Hence also the energy states for different surfaces separate to

$$\tilde{\epsilon}_1^2 = (\tilde{\mu}_p + \tilde{\alpha})^2 + |\Delta_1|^2 \tag{130}$$
$$\tilde{\epsilon}_N^2 = (\tilde{\mu}_p - \tilde{\alpha})^2 + |\Delta_N|^2. \tag{131}$$

The eigenstates of the bottom layer $n = 1$ can be then solved from the two components of Eq. (128)

$$\tilde{\epsilon}_1 A^+ - (\tilde{\mu}_p + \tilde{\alpha}) A^+ = \Delta_1 B^+ \tag{132}$$

$$\tilde{\epsilon}_1 B^+ + (\tilde{\mu}_p + \tilde{\alpha}) B^+ = \Delta_1^* A^+ \tag{133}$$

and the normalization

$$(A^+)^2 + (B^+)^2 = 1.$$

The equation (132) gives with the normalization constraint

$$(A^+)^2 = \frac{\Delta_1^2}{\Delta_1^2 + \tilde{\epsilon}_1^2 + (\tilde{\mu}_p + \tilde{\alpha})^2 - 2\tilde{\epsilon}_1(\tilde{\mu}_p + \tilde{\alpha})}.$$

After substituting Δ_1 from Eq. (130) we get

$$(A^+)^2 = \frac{1}{2}\left(1 + \frac{\tilde{\mu}_p + \tilde{\alpha}}{\tilde{\epsilon}}\right).$$

So the eigenstates for $n = 1$ in the flat band limit are $A^+ = U_1$ and $B^+ = V_1$ or $A^+ = V_1$ and $B^+ = U_1$ with

$$U_1 = \frac{1}{\sqrt{2}}\left[1 + \frac{\tilde{\mu}_p + \tilde{\alpha}}{\tilde{\epsilon}_1}\right]^{\frac{1}{2}} \quad \text{and} \quad V_1 = \frac{1}{\sqrt{2}}\left[1 - \frac{\tilde{\mu}_p + \tilde{\alpha}}{\tilde{\epsilon}_1}\right]^{\frac{1}{2}} \tag{134}$$

Similarly for $n = N$ we get the eigenstates using Eqs. (129) and (131) to be $A^- = U_N$ and $B^- = V_N$ or $A^- = V_N$ and $B^- = U_N$, where

$$U_N = \frac{1}{\sqrt{2}}\left[1 + \frac{\tilde{\mu}_p - \tilde{\alpha}}{\tilde{\epsilon}_N}\right]^{\frac{1}{2}} \quad \text{and} \quad V_N = \frac{1}{\sqrt{2}}\left[1 - \frac{\tilde{\mu}_p - \tilde{\alpha}}{\tilde{\epsilon}_N}\right]^{\frac{1}{2}}. \tag{135}$$

We take next the general self-consistency equation (127) and write it for the surface states. Since the surface states are localized we have $k = 0$. Consider first the trace in Eq. (127) for $n = N$:

$$\begin{aligned}
\mathrm{Tr}[\hat{u}_N(\mathbf{p},0)\hat{v}_N^*(\mathbf{p},0)] =& \alpha_N^+ \beta_N^{*+} + \alpha_N^- \beta_N^{*-} \\
=& \frac{|C|^2}{2}[\mathcal{O}(p^{N-1}) + \zeta_1^e \zeta_1^h A^- B^- + A^- B^-] \\
\to& \frac{|C|^2}{2} A^- B^-
\end{aligned}$$

in the limit $N \to \infty$. Above we made an approximation

$$1 + \zeta_1^e \zeta_1^h \approx 1, \tag{136}$$

since $\zeta_1^{e,h}$ are proportional to ϵ, μ, α and γ_4. In a similar way we get for $n = 1$

$$\mathrm{Tr}[\hat{u}_1(\mathbf{p},0)\hat{v}_1^*(\mathbf{p},0)] = \alpha_1^+\beta_1^{*+} + \alpha_1^-\beta_1^{*-} = \frac{|C|^2}{2}A^+B^+. \tag{137}$$

Using the definition of the Fermi function (97) we also find through a straightforward calculation

$$1 - 2f(E_{\mathbf{p},k}) = \tanh\frac{\epsilon}{2T} \tag{138}$$

so the self-consistency equation for the order parameter on the surface is

$$\Delta_{\underset{N}{1}} = 2W \int\limits_{p<p_{FB}} \frac{\mathrm{d}^2p}{(2\pi\hbar)^2}|C|^2 U_{\underset{N}{1}} V_{\underset{N}{1}} \tanh\frac{\epsilon}{2T}. \tag{139}$$

We get the normalization constant $|C|^2 = (1 - v_F^2p^2/\gamma_1^2)/d$ from the definitions (117) and (118) by requiring

$$d\sum_{n=1}^{N}[|\alpha_n^+|^2 + |\beta_n^+|^2 + |\alpha_n^-|^2 + |\beta_n^-|^2] = 1. \tag{140}$$

The calculation is presented in Appendix C. Using the results (134) and (135) for $U_{\underset{N}{1}}$ and $V_{\underset{N}{1}}$ we get

$$\begin{aligned}\Delta_{\underset{N}{1}} =& 2W \int\limits_{p<p_{FB}} \frac{\mathrm{d}^2p}{(2\pi\hbar)^2} \frac{(1 - v_F^2p^2/\gamma_1^2)^2\Delta_{\underset{N}{1}}}{\sqrt{(\mu_p \pm \alpha)^2 + |\Delta_{\underset{N}{1}}|^2(1 - v_F^2p^2/\gamma_1^2)^2}} \\ &\times \tanh\frac{\sqrt{(\mu_p \pm \alpha)^2 + |\Delta_{\underset{N}{1}}|^2(1 - v_F^2p^2/\gamma_1^2)^2}}{2T}.\end{aligned} \tag{141}$$

We see immediately that for $\mu_p = 0$ the order parameters for different surfaces are determined by the same equation, so $\Delta_1(\alpha) = \Delta_N(\alpha)$. The numerical solution of Eq. (141) as a function of α is plotted in Fig. 14 for $\mu_p = 0$. The effects of non-zero chemical potential and the order parameter γ_4 are demonstrated in Figs. 15 and 16 respectively. The figures contain also values for $\Delta_{1,N}$ that are numerically solved from Eq. (127) using the Hamiltonian (108), where I used as an Ansatz the solution for Eq. (141). In all the plots $T = 0$ and $\gamma_3 = 0$.

Equation (141) does not yield a non-trivial solution for an arbitrary amount of doping. For $\gamma_4 = 0$, the superconductivity is destroyed if the term $|\mu \mp \alpha|$ exceeds the critical doping $\mu_c = 2\Delta(T = 0)/3$ [15]. Below we derive explicitly that in our case $\Delta(T = 0) = g/(8\pi)$, which gives $\mu_c = g/(12\pi)$. In Fig. 14 we have $g = 0.5\,\gamma_1$, so the critical doping in the plots is $\mu_c = 1/(24\pi)\gamma_1 \approx$

$0.0133\,\gamma_1$. Let us consider first Fig. 14 where $\mu_p = 0$. The black dash-dotted plot of Eq. (141) is non-zero only between the limiting values of μ_c as excepted. This holds also for the numerical solutions. The solid red and blue lines are the flat band solutions that are calculated with $N = 100$. Reducing the number of layers to $N = 50$ did not produce any distinguishable difference to the solution with $N = 100$, so already $N = 50$ is enough to produce the flat band solution. For the dashed lines the number of layers is $N = 20$. It seems that for Δ_1 the cutoff doping is even below the analytical μ_c, at $\alpha \approx 0.01\,\gamma_1$. In the vicinity of the points $\alpha = \pm 0.01\,\gamma_1$ there occurs also drops in Δ_N. These points were in all the Figs. 14-16 hard to handle for the numerics. There are probably several solutions for the self-consistency equation, and with $N = 20$ the convergence to the flat band solution was uncertain at these values values of α. With $N = 100$ these kinds of problems did not occur, though this calculation was carried out only once, since the time required for the numerics grows quickly with an increasing N.

As noticed already above, Eq. (141) gives the same values $\Delta_1(\alpha) = \Delta_N(\alpha)$ if $\mu_p = 0$. Surprisingly this is not the case with the numerical solution: even in the flat band limit the shapes of the functions $\Delta_1(\alpha)$ and $\Delta_N(\alpha)$ differ. We see in Fig. 14 that Δ_1 is clearly narrower than Δ_N. Additionally Δ_1 is almost flat just around $\alpha = 0$ whereas Δ_N is more parabolic. The difference in the shapes is only emphasized when $N = 20$. There is no explanation for this asymmetry in the theory. When $\gamma_4 = \gamma_3 = 0$ the top and bottom layers are distinguished in the following way (see Fig. 5): in the bottom only the atoms from sublattice B are affected by interlayer hopping γ_1 while the atoms A do not interact with the upper layer. On the top layer only the A atoms are coupled by γ_1 to the layer below and the B atoms interact only within the layer. The roles of A and B can be changed by taking $\alpha \to -\alpha$, which implies $\Delta_1(\alpha) = \Delta_N(-\alpha)$. This is, however, not satisfied in the numerical solution. Neither of the numerically calculated Δ_1 or Δ_N follows the analytical approximation very well, except for $\alpha = 0$. Both Δ_1 and Δ_N are more flat near $\alpha = 0$ than the analytical solution, but drop then suddenly to zero. The numerical values for $\Delta_{1,N}$ are nevertheless symmetric in α and reach their maximum values in $\alpha = 0$ like the analytical approximation. For $N = 20$ the amplitudes of $\Delta_{1,N}$ do not quite reach the flat band values.

The numerical solutions with $\gamma_3 = \gamma_4 = 0$ and the analytical approximation with $\mu = 0.01$ are presented in Fig. 15. The effect of the chemical potential in Eq. (141) is clearly only a shift of α, since $\Delta_{\substack{1\\N}} = \Delta(\mu \mp \alpha)$. Note that $\mu_p = -\mu$ for $\gamma_4 = 0$. Hence the maximum of Δ_1 is at $\alpha = -\mu$ and the maximum of Δ_N is at $\alpha = \mu$. We see that the numerical solutions behave in the same way. For both Δ_1 and Δ_N there are small ranges of alpha where the order parameters

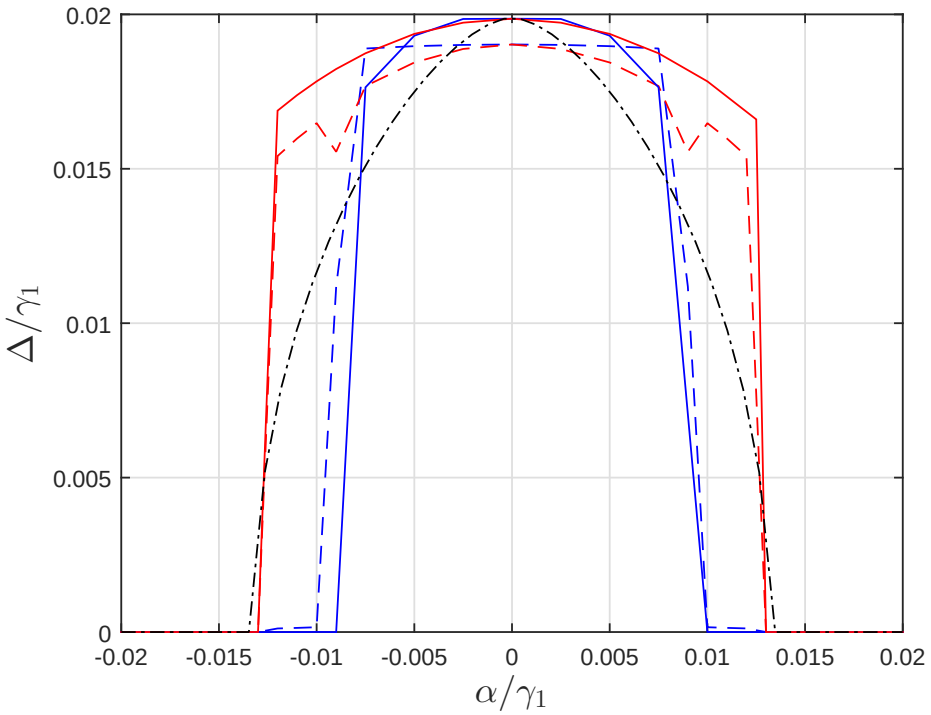

Figure 14: Numerical and analytical solutions for the surface order parameters. The blue lines are values for Δ_1 and the red lines correspond to Δ_N. Here I set $\mu = 0$, $\gamma_3 = \gamma_4 = 0$ and $T = 0$ with $g = 0.5\,\gamma_1$. Dashed lines are the numerical solutions, where the number of layers is $N = 20$ and the solid lines are calculated for $N = 100$. The black dash-dotted line is the numerically solved analytical approximation (141).

suddenly have non-zero values even though the main part of the curve has already reached zero. In these values the convergence of the code was very slow and the peculiar values may be another solution for the self-consistency equation or just a numerical issue, as discussed above. The main result of this analysis is that for a non-zero staggering potential doping can produce very asymmetric order parameters for different surfaces of rhombohedral graphite.

If the hopping γ_4 is included, Eq. (141) gives different values for Δ_1 and Δ_N (see Fig. 16, solid lines). The values are shifted such that Δ_1 reaches its maximum at $\alpha \simeq -0.01$ and Δ_N at $\alpha \simeq 0.01$. The curves are also lower and wider than in the absence of γ_4, but the symmetry $\Delta_1(\alpha) = \Delta_N(-\alpha)$ remains. The changes in the numerically calculated order parameters are similar than in the analytical case. With non-zero γ_4 the analytical solution for Δ_N seems to fit

even better to the numerics as with $\gamma_4 = 0$. On the other hand the difference between analytically and numerically obtained Δ_1:s is enhanced.

Let us finally solve the order parameter Δ at zero temperature in the flat band limit, i.e., when $\gamma_4 = 0$ and $\xi_p = 0$. Assuming zero doping $\mu = 0$ and vanishing staggering potential $\alpha = 0$ we get

$$\Delta(T=0) = \frac{W}{d} \int\limits_{p<p_{FB}} \frac{\mathrm{d}^2 p}{(2\pi\hbar)^2}(1 - v_F^2 p^2/\gamma_1^2). \tag{142}$$

Here we first divided both sides of Eq. (141) by Δ and then set $T \to 0$. We also needed the fact $lim_{x\to\infty} \tanh x = 1$. Next we change the variables to polar coordinates and remember that $p_{FB} = \gamma_1/v_F$. Then

$$\Delta(T=0) = \frac{W}{d2\pi\hbar^2} \int\limits_0^{p_{FB}} (p - p^3/p_{FB}^2) = \frac{g}{8\pi}, \tag{143}$$

where

$$g = \frac{(W/d)\gamma_1^2}{v_F^2\hbar^2} \tag{144}$$

is the coupling energy. Hence the order parameter and then critical temperature depend *linearly* on the coupling parameter. This differs significally from the BCS theory, where $\Delta \sim \exp(-1/(W\nu(0)))$. Therefore, the presence of a flat band can lead to a very high superconducting state transition temperature.

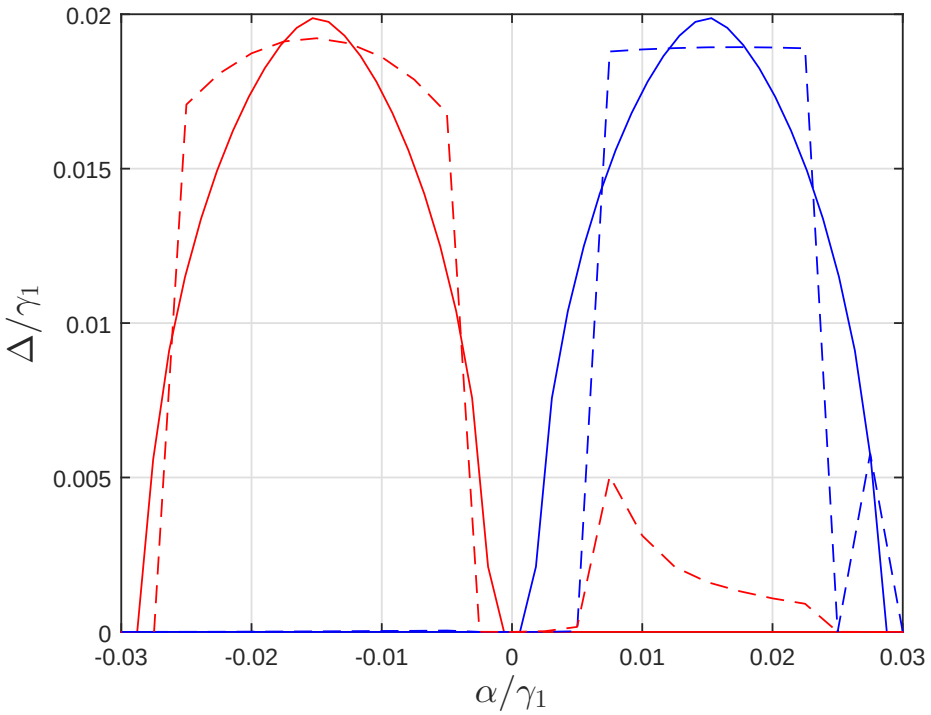

Figure 15: Surface order parameters with $\mu = 0.015\,\gamma_1$. The values for Δ_1 are plotted with blue and Δ_N with red. Here we assume $\gamma_3 = \gamma_4 = 0$, $T = 0$ and $g = 0.5\,\gamma_1$. Solid lines are the values given by the analytical approximation (141) and dashed lines are the numerically solved values for $N = 20$.

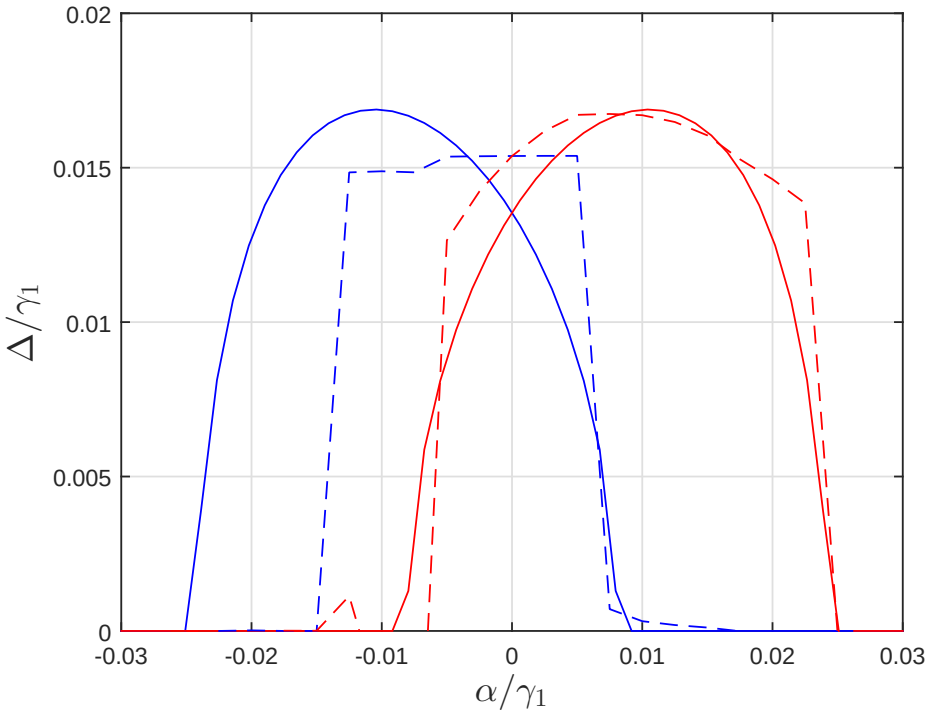

Figure 16: The effect of the hopping $\gamma_4 = 0.044\,\text{eV}$ to the surface order parameters. Blue lines are Δ_1 and red ones are Δ_N. Again solid lines are the analytical values from Eq. (141) and the dashed lines are the numerical solutions for $N = 20$. The essential parameters are $\mu = 0$, $\gamma_3 = 0$, $T = 0$ and $g = 0.5\,\gamma_1$.

7 Conclusion

The field of topological materials is young but fast developing. New classifications for topological materials are constantly made as the understanding of the different topological invariants grows. A lot of study is required until the topological materials can be capitalized on applications, but the opportunities seem already exciting. Although graphene is one of the first realizations of topological materials and it has been under intensive investigation, it is not yet thoroughly explored. Especially graphene based materials, such as different types of graphite or graphene modified by defects, can manifest the topology of graphene in interesting ways.

The analytical and numerical calculations in Sec. 4 show that even though the staggering potential breaks the topological protection of the surface states, something of the flat band remains. In Fig. 10 we see that the major effect of α is the breaking of the degeneracy at $p = 0$ while the shape of the band does not essentially change. With suitable doping one of the two bands could be lifted to zero energy, which would produce the flat band phenomena to the other surface while the other would not contribute to the low-energy limit.

The asymmetry of the surfaces arises in a concrete way in Sec. 6, where we study the effect of α to the surface superconductivity. Especially, if there is a non-zero chemical potential, the superconductivity may occur only on one surface. Perhaps the most interesting observation in Fig. 14 is the fact, that the shapes of numerically calculated Δ_1 and Δ_N as a function of α differ while the analytical approximation gives the same form for both Δ:s. Since the system has the symmetry $\Delta_1(\alpha) = \Delta_N(-\alpha)$ as explained above, the asymmetry must come from the numerics. It is not clear how, since the Hamiltonian has the same symmetry as the system and we used the analytical approximation (141), which is symmetric, as an Ansatz. It is possible that there happens a spontaneous symmetry breaking and that the obtained numerical solution corresponds to a metastable state. The next step would be to study if there is a symmetric solution by forcing the Δ:s to be the same after every step of iteration. It there is such a state one should calculate the energy expectation values for both symmetric and asymmetric states and compare which one corresponds to lower energy.

The presence of the staggering potential also breaks the degeneracy at $p = 0$ and produces band crossings. The analytical approximation (123) fits the numerical solutions well for $p < 0.8\,\gamma_1$ with different values of α and μ. With proper combinations of α and μ the dispersion can be modified: for example in Fig. 13 choosing $\alpha = \mu = 0.015\,\gamma_1$ suppresses the superconductivity on the layer Δ_N and produces a gapped flat band.

8 Appendix

A Adiabatic approximation

This appendix follows lecture notes [24]. In an adiabatic process the parameters $\mathbf{R}(t)$ of H change very slowly in time. Consider first the case when the Hamiltonian depends directly on time, i.e., the dependence of the parameters $\mathbf{R}$ is omitted. The time evolution of a state is given by the Schrödinger equation

$$i\hbar \frac{\mathrm{d}}{\mathrm{d}t} |\psi(t)\rangle = H(t) |\psi(t)\rangle . \tag{145}$$

Since we assume the eigenstates $|n(t)\rangle$ to form an orthogonal basis, the state $|\psi(t)\rangle$ solving the Schrödinger equation can be expanded as

$$|\psi(t)\rangle = \sum_n c_n(t) e^{i\delta_n} |\psi_n(t)\rangle , \tag{146}$$

where

$$\delta_n(t) = -\frac{1}{\hbar} \int_0^t \mathrm{d}t' \epsilon_n(t'). \tag{147}$$

If the system is assumed initially to be on the state $\psi_i(0)$, we should have $c_n(0) = \delta_{ni}$. The time dependence of these coefficients can be obtained by substituting the form (146) to the Schrödinger equation (145). After a straightforward calculation a condition for the coefficients c_n is

$$\frac{\mathrm{d}c_n}{\mathrm{d}t} = -\sum_m e^{i(\delta_m - \delta_n)} \langle \psi_n \,|\, \dot{\psi}_m \rangle \, c_m. \tag{148}$$

One can show that taking the time derivative of the Schrödinger equation eventually leads to

$$\langle \psi_n | \frac{\partial H}{\partial t} |\psi_m\rangle = (E_m - E_n) \langle \psi_n \,|\, \dot{\psi}_n \rangle . \tag{149}$$

Using this equation we get from Eq. (148)

$$\frac{\mathrm{d}c_n}{\mathrm{d}t} = -\langle \psi_n \,|\, \dot{\psi}_n \rangle \, c_n + \sum_{m \neq n} e^{i(\delta_m - \delta_n)} \frac{\langle \psi_n | \, \partial H/\partial t \, |\psi_m\rangle}{E_n - E_m} c_m. \tag{150}$$

If we now assume that the Hamiltonian depends on time very weakly, the terms $\langle \psi_n | \, \partial H/\partial t \, |\psi_m\rangle$ can be neglected. This assumption is called the *adiabatic approximation*. Then

$$\frac{\mathrm{d}c_n}{\mathrm{d}t} = -\langle \psi_n \,|\, \dot{\psi}_n \rangle \, c_n. \tag{151}$$

The inner product is purely imaginary, since time derivation of $1 = \langle \psi_n \,|\, \psi_n \rangle$ gives

$$0 = \langle \psi_n \,|\, \dot{\psi}_n \rangle + \langle \dot{\psi}_n \,|\, \psi_n \rangle = \langle \psi_n \,|\, \dot{\psi}_n \rangle + \langle \psi_n \,|\, \dot{\psi}_n \rangle^* .$$

Now the solution to equation (151) is

$$c_n(t) = e^{i\gamma_n} c_n(0) = e^{i\gamma_n} \delta_{ni} \tag{152}$$

with

$$\gamma_n(t) = i \int_{t_0}^{t} \mathrm{d}t \, \langle \dot{\psi}_n \,|\, \psi_n \rangle \tag{153}$$

which is a real number.

If the Hamiltonian depends on time via parameters $\mathbf{R}(t)$, the time derivative of the eigenstate can be written as

$$|\dot{\psi}_n(\mathbf{R}(t))\rangle = \sum_k \frac{\mathrm{d}R_k}{\mathrm{d}t} \frac{\partial}{\partial R_k} |\psi_n(\mathbf{R}(t))\rangle = \frac{\mathrm{d}\mathbf{R}}{\mathrm{d}t} \cdot \nabla_{\mathbf{R}} |\psi_n(\mathbf{R}(t))\rangle . \tag{154}$$

This gives for the geometric phase (153)

$$\gamma_n(t) = i \int_{t_0}^{t} \mathrm{d}t \frac{\mathrm{d}\mathbf{R}}{\mathrm{d}t} \cdot \langle \dot{\psi}_n \,|\, \nabla_{\mathbf{R}} \,|\, \psi_n \rangle . \tag{155}$$

We can now substitute the coefficients (152) back to Eq. (146). So at time t the system is in the state

$$|\psi(\mathbf{R}(t))\rangle = \sum_n e^{i\gamma_n} \delta_{ni} e^{i\delta_n} |\psi_n(\mathbf{R}(t))\rangle = e^{i\gamma_i} e^{i\delta_i} |\psi_i(\mathbf{R}(0))\rangle . \tag{156}$$

Hence the system stays in the initial state through an adiabatic transformation up to a phase factor that consists of the dynamical and geometrical parts. The existence of the phase leads to various quantum effects and we discuss the consequences of the geometrical phase in Sec. 2.

B Consistency of Ansatz

We need to show that the Ansatz (67) solves Eq. (66) for an arbitrary n up to order $\mathcal{O}(\epsilon^2, \mu^2, \alpha^2, (\gamma_4/\gamma_0)^2)$. Equation (66) can be written as a matrix equation

$$\begin{pmatrix} \alpha\psi_n^A + v_F p_- \psi_n^B \\ v_F p_+ \psi_n^A - \alpha\psi_n^B \end{pmatrix} - \gamma_1 \Big[e^{i\pi/6} \begin{pmatrix} 0 \\ \psi_{n+1}^B \end{pmatrix} + e^{-i\pi/6} \begin{pmatrix} \psi_{n-1}^A \\ 0 \end{pmatrix} \Big]$$
$$+ \frac{\gamma_4}{\gamma_0} v_F \Big[e^{i\pi/6} v_F p_- \begin{pmatrix} \psi_{n+1}^A \\ \psi_{n+1}^B \end{pmatrix} + e^{-i\pi/6} v_F p_+ \begin{pmatrix} \psi_{n-1}^A \\ \psi_{n-1}^B \end{pmatrix} \Big] = (\epsilon + \mu) \begin{pmatrix} \psi_n^A \\ \psi_n^B \end{pmatrix}. \quad (157)$$

We consider the upper and the lower rows separately. Taking the upper row and substituting the Ansatz leads to a very similar equation as Eq. (72):

$$\begin{aligned} & v_F p e^{-i\phi} e^{i(\phi-\pi/6)(n-1-\frac{N}{2})} e^{i\phi} \left[\left(\frac{v_F p}{\gamma_1} \right)^{n-1} \zeta_2 A_+ + \left(\frac{v_F p}{\gamma_1} \right)^{N-n} A_- \right] \\ & - \gamma_1 e^{-i\pi/6} e^{i(\phi-\pi/6)(n-2-\frac{N}{2})} e^{i\phi} \left[\left(\frac{v_F p}{\gamma_1} \right)^{n-2} \zeta_2 A_+ + \left(\frac{v_F p}{\gamma_1} \right)^{N-n+1} A_- \right] \\ & + \frac{\gamma_4}{\gamma_0} v_F p e^{-i(\phi-\pi/6)} e^{i(\phi-\pi/6)(n-\frac{N}{2})} \left[\left(\frac{v_F p}{\gamma_1} \right)^{n} A_+ + \left(\frac{v_F p}{\gamma_1} \right)^{N-n-1} \zeta_1 A_- \right] \\ & + \frac{\gamma_4}{\gamma_0} v_F p e^{i(\phi-\pi/6)} e^{i(\phi-\pi/6)(n-2-\frac{N}{2})} \left[\left(\frac{v_F p}{\gamma_1} \right)^{n-2} A_+ + \left(\frac{v_F p}{\gamma_1} \right)^{N-n+1} \zeta_1 A_- \right] \\ & = (\epsilon + \mu - \alpha) e^{i(\phi-\pi/6)(n-1-\frac{N}{2})} \left[\left(\frac{v_F p}{\gamma_1} \right)^{n-1} A_+ + \left(\frac{v_F p}{\gamma_1} \right)^{N-n} \zeta_1 A_- \right]. \end{aligned} \quad (158)$$

Again the phase factors cancel out. To simplify the notations, we switch to units where $v_F = \gamma_1 = 1$. Then rearranging the terms in Eq. (158) gives

$$\left[p^n \zeta_2 - p^{n-2} \zeta_2 + \frac{\gamma_4}{\gamma_0} (p^{n+1} + p^{n-1}) - (\epsilon + \mu - \alpha) p^{n-1} \right] A_+$$
$$+ \left[\cancel{p^{N-n+1}} - \cancel{p^{N-n+1}} + p^{N-n} \frac{\gamma_4}{\gamma_0} \zeta_1 + p^{N-n+2} \frac{\gamma_4}{\gamma_0} \zeta_1 - (\epsilon + \mu - \alpha) p^{N-n} \zeta_1 \right] A_- = 0$$

Substitution of definitions (68) for $\zeta_{\frac{1}{2}}$ into above equation gives for the coefficient of A_+ after some algebra

$$\frac{p_{n-1}(\epsilon + \mu - \alpha)}{p^2 - 1} \left[p^2 - 1 - (p^2 - 1) \right]$$
$$+ \frac{\gamma_4}{\gamma_0} p^{n-1} \left[-p^2 \frac{p^2 + 1}{p^2 - 1} + \frac{p^2 + 1}{p^2 - 1} + p^2 + 1 \right] = 0,$$

which turns out to be exactly zero. For the coefficient of A_- we get

$$\begin{aligned}
&\frac{p^{N-n+1}}{p^2-1}\frac{\gamma_4}{\gamma_0}(\epsilon+\mu+\cancel{\alpha})(p^2+1)-\frac{p^{N-n+1}}{p^2-1}\left(\frac{\gamma_4}{\gamma_0}\right)^2(p^2+1)^2\\
&-\frac{p^{N-n+1}}{p^2-1}(\epsilon+\mu-\alpha)(\epsilon+\mu+\alpha)+\frac{p^{N-n+1}}{p^2-1}\frac{\gamma_4}{\gamma_0}(\epsilon+\mu-\cancel{\alpha})(p^2+1)\\
=&\frac{2p^{N-n+1}}{p^2-1}\frac{\gamma_4}{\gamma_0}(\epsilon+\mu)(p^2+1)-\frac{p^{N-n+1}}{p^2-1}\left(\frac{\gamma_4}{\gamma_0}\right)^2(p^2+1)^2\\
&-\frac{p^{N-n+1}}{p^2-1}((\epsilon+\mu)^2-\alpha^2)\\
\approx&0,
\end{aligned}$$

if we neglect everything that is of a second order in energy or $\gamma_4/\gamma_0 \ll 1$. The low energy limit is valid if we also demand $\alpha \ll \gamma_1$ and $\mu \ll \gamma_1$. For our purposes this is a reasonable limitation. In graphite the energy scale that determines the essential properties of the material is $\gamma_1 = 1$ in our units. If the on-site potential α or the chemical potential μ were of the same order, the behaviour of the system would be drastically changed and our low-energy approximation would not be valid any more.

For the lower row in Eq. (157) the calculations and necessary approximations are very similar to ones done above. Now just the coefficient of A_- is exactly zero and the term proportional to A_+ is zero up to second order in energy and γ_4/γ_0. So the Ansatz is valid for a general n in the low energy limit.

C Normalization constant

Let us again use the units where $\gamma_1 = v_F = 1$. Substitution of the squares of the absolute values for all the coefficients $\alpha_n^{\pm}$, $\beta_n^{\pm}$ in Eq. (140) gives a constraint

$$\begin{aligned} 1 = \frac{|C|^2 d}{2} \sum_{n=1}^{N} \Big[& p^{2(n-1)} + (\zeta_1^e)^2 p^{2(N-n)} (A^-)^2 + 2p^{N-1}(\zeta_1^e + \zeta_2^e) A^+ A^- \\ & + p^{2(N-n)} + (\zeta_1^h)^2 p^{2(N-n)} (B^-)^2 + (\zeta_2^e)^2 p^{2(n-1)} (A^+)^2 \\ & + (\zeta_2^h)^2 p^{2(n-1)} (B^+)^2 + 2p^{N-1}(\zeta_1^h + \zeta_2^h) B^+ B^- \Big]. \end{aligned} \tag{159}$$

We see from the definition (119) that every term in $\check{\zeta}_{\frac{1}{2}}$ is proportional to ϵ, α, μ or (γ_4/γ_0). Then if we neglect everything that is of second order in any of the parameters mentioned above, we can set $(\zeta_i^p)^2 = 0$ for $i = 1,2$, $p = e,h$. Then substituting Def. (119) into remaining terms of Eq. (159) gives

$$\begin{aligned} 1 = & \frac{|C|^2 d}{2} \sum_{n=1}^{N} \Big[p^{2(n-1)} + p^{2(N-n)} + 2\frac{\xi_p}{p^2 - 1} \Big((\epsilon + \mu) A^+ A^- \\ & + (-\epsilon + \mu) B^+ B^- - (\gamma_4/\gamma_0)(p^2 - 1)(A^+ A^- + B^+ B^-) \Big) \Big]. \end{aligned}$$

In the low-energy limit we have also $\xi_p \ll \gamma_1$, so also the last terms proportional to $A^{\pm}$, $B^{\pm}$ vanish. Thus the normalization constraint reduces to

$$1 = \frac{|C|^2 d}{2} \sum_{n=1}^{N} \Big[p^{2(n-1)} + p^{2(N-n)} \Big]. \tag{160}$$

The remaining sums are geometric so they can be easily solved. They both give as a result $(1 - p^2)^{-1}$ so the normalization constant is

$$|C|^2 = (1 - p^2)/d. \tag{161}$$

or in the original units

$$|C|^2 = (1 - v_F^2 p^2/\gamma_1^2)/d. \tag{162}$$

It is good to notice that this result is valid already in the low-energy limit. Here we have not made any flat band assumptions.

References

[1] A Ballestar, J Barzola-Quiquia, T Scheik e, and P Esquinazi. Josephson-coupled superconducting regions embedded at the interfaces of highly oriented pyrolytic graphite. *New J. Phys.*, 15(2):023024, 2013.

[2] B. Andrei Bernevig and Taylor L. Hughes. *Topological Insulators and Topological Superconductors*. Princeton University Press, Princeton, New Jersey, 2013.

[3] A. H. Castro Neto, F. Guinea, N. M. R. Peres, K. S. Novoselov, and A. K. Geim. The electronic properties of graphene. *Rev. Mod. Phys.*, 81:109–162, Jan 2009.

[4] R. Ricardo da Silva, J. H. S. Torres, and Y. Kopelevich. Indication of superconductivity at 35 k in graphite-sulfur composites. *Phys. Rev. Lett.*, 87:147001, Sep 2001.

[5] P. Esquinazi, N. García, J. Barzola-Quiquia, P. Rödiger, K. Schindler, J.-L. Yao, and M. Ziese. Indications for intrinsic superconductivity in highly oriented pyrolytic graphite. *Phys. Rev. B*, 78:134516, Oct 2008.

[6] Vitaly L. Ginzburg. Nobel Lecture: On superconductivity and superfluidity (what i have and have not managed to do) as well as on the "physical minimum" at the beginning of the xxi century*. *Rev. Mod. Phys.*, 76:981–998, Dec 2004.

[7] GianMichele Graf and Marcello Porta. Bulk-edge correspondence for two-dimensional topological insulators. *Commun. Math. Phys.*, 324(3):851–895, 2013.

[8] F. D. M. Haldane. Model for a Quantum Hall Effect without Landau Levels: Condensed-Matter Realization of the "Parity Anomaly". *Phys. Rev. Lett.*, 61:2015–2018, Oct 1988.

[9] Tero T. Heikkilä. *The Physics of Nanoelectronics*. Oxford University Press, 2013.

[10] Tero T. Heikkilä and Grigori E. Volovik. Flat bands as a route to high-temperature superconductivity in graphite. arXiv:1504.05824 [cond-mat.mtrl-sci], Apr 2015.

[11] Tero T. Heikkilä and Grigori E. Volovik. Nexus and dirac lines in topological materials. arXiv:1504.05824 [cond-mat.mtrl-sci], May 2015.

[12] T.T. Heikkilä, N.B. Kopnin, and G.E. Volovik. Flat bands in topological media. *JETP Letters*, 94(3):233–239, 2011.

[13] T.T. Heikkilä and G.E. Volovik. Dimensional crossover in topological matter: Evolution of the multiple dirac point in the layered system to the flat band on the surface. *JETP Letters*, 93(2):59–65, 2011.

[14] C. L. Kane. *Topological Band Theory and the $\mathbb{Z}_2$ Invariant*. Elsevier B. V., 2013. First chapter in the book *Topological Insulators* by Marcel Franz and Laurens Molenkamp.

[15] N. B. Kopnin, T. T. Heikkilä, and G. E. Volovik. High-temperature surface superconductivity in topological flat-band systems. *Phys. Rev. B*, 83:220503, Jun 2011.

[16] N. B. Kopnin and T. T. Heikkilä. Surface superconductivity in rhombohedral graphite. *arXiv:1210.7075v2 [cond-mat.supr-con]*, 2012.

[17] Yuli V. Nazarov and Jeroen Danon. *Advanced Quantum Mechanics*. Cambridge University Press, 2013.

[18] Bitan Roy. *Aspects of interacting electrons on Graphene Honeycomb Lattice*. PhD thesis, Simon Fraser University, 2011.

[19] T. Scheike, W. Böhlmann, P. Esquinazi, J. Barzola-Quiquia, A. Ballestar, and A. Setzer. Can doping graphite trigger room temperature superconductivity? Evidence for granular high-temperature superconductivity in water-treated graphite powder. *Adv. Mat.*, 24(43):5826–5831, 2012.

[20] Jörg Schmalian. Failed theories of superconductivity. *arXiv:1008.0447 [physics.hist-ph]*, 2010.

[21] John Stillwell. *Geometry of Surfaces*. Springer Science & Business Media, 1992.

[22] D. J. Thouless, M. Kohmoto, M. P. Nightingale, and M. den Nijs. Quantized Hall Conductance in a Two-Dimensional Periodic Potential. *Phys. Rev. Lett.*, 49:405–408, Aug 1982.

[23] Michael Tinkhman. *Introduction to Superconductivity*. Dover Publications, Inc., Mineola, New York, second edition edition, 1996.

[24] Kimmo Tuominen. Quantum mechanics II. `http://theory.physics.helsinki.fi/~qmii/kvantti2_notes.pdf`. Lecture notes.

[25] Ari M. Turner and Ashvin Vishwanath. *Beyond Band Insulators: Topology of Semimetals and Interacting Phases*. Elsevier B. V., 2013. Chapter 11 in the book *Topological Insulators* by Marcel Franz and Laurens Molenkamp.

[26] Di Xiao, Ming-Che Chang, and Qian Niu. Berry phase effects on electronic properties. *Rev. Mod. Phys.*, 82:1959–2007, Jul 2010.